To appear in the *Journal of Hydraulic Research*
Vol. 00, No. 00, Month 20XX, 1–16

Research paper

Experimental characterization of bed evolution and water surface elevation by consecutive dambreaks using Kinect device

JOSE SEGOVIA-BURILLO (IAHR Member), PhD student, *I3A, University of Zaragoza, Zaragoza, Spain*, *Email: jsegovia@unizar.es (author for correspondence)*

SERGIO MARTÍNEZ-ARANDA, Professor, *I3A, University of Zaragoza, Zaragoza, Spain*, *Email: sermar@unizar.es*

MARIO MORALES-HERNÁNDEZ (IAHR Member), Professor,*I3A, University of Zaragoza, Zaragoza, Spain*,

JAVIER FERNÁNDEZ-PATO, Researcher, *Estación Experimental Aula Dei, CSIC, Zaragoza, Spain; ARAID Foundation, Zaragoza, Spain*,

PILAR GARCÍA-NAVARRO (IAHR Member), Full Professor, *I3A, University of Zaragoza, Zaragoza, Spain*,

Running Head: MEASUREMENTS OF BED EVOLUTION AND WATER SURFACE ELEVATION

ABSTRACT

Extreme phenomena such as dambreak flows are of great interest in hydraulic engineering due to their destructive power. Dambreak waves can cause severe morphological damage to channels and erodible beds through high-velocity water flows. Numerical models of unsteady erodible shallow flow must be properly validated to become reliable predictive tools. In this work, a novel set of laboratory experiments is presented in which bed evolution and water surface elevation are measured in a 2D flume subjected to consecutive dambreak flows. The experiments were conducted for various geometries and obstacle configurations. Bedform dynamics were measured using an RGB-D camera sensor over the experimental region. The results show that bedload transport rates are strongly influenced by flume geometry and flow conditions. These results provide valuable insights into bedload transport dynamics during dambreak flows and can be used to improve the design of numerical models for erosive shallow water simulations.

Keywords: experimental setup free shallow surface 2D datasheet sand bed erosion structure scouring non-intrusive measurements

This paper was published in the *Journal of Hydraulic Research*.
Please cite the Version of Record: `https://doi.org/10.1080/00221686.2025.2602056`

1 Introduction

Understanding the interaction between free surface water flows and erodible bed layers is fundamental to natural processes such as coastal erosion, river sediment transport, and dambreak events (Cao et al., 2004; Wu, 2007; Zech et al., 2008). When rapid flows, often associated with mountainous areas or extreme phenomena, exert hydraulic forces on the bed elements, if the aggregation state is not strong enough, particles may detach and be transported either suspended in the fluid or as bed load, eventually settling downstream. A critical aspect of this process is local scour, where flow acceleration around obstacles leads to concentrated erosion (Bento et al., 2022b; Breusers and Raudkivi, 2020; Lu et al., 2013; Melville and Raudkivi, 1996). These phenomena can have significant environmental and structural impacts, causing bed degradation, sediment displacement, alterations in the fauna and flora, and alterations in flow patterns (Teraguchi et al., 2011). Specifically, controlled dambreak laboratory experiments are often used to validate free-surface numerical models under unsteady, rapidly-varied flow conditions (Wu and Wang, 2007; Zech et al., 2008). This is due to their experimental and simulation simplicity and their ability to generate destructive, high-velocity waves (Capart et al., 2007; Yochum et al., 2008).

Even though dambreak waves are frequently treated as one-dimensional phenomena (Ferreira et al., 2005; Goutière et al., 2008; Liu et al., 2018; Martínez-Aranda et al., 2019; Rosatti and Begnudelli, 2010; Wu and Wang, 2007), rigid structures (often human-made) in the flow path can further complicate dynamics by altering the velocity field and make it necessary to use a 2D representation. This flow dynamics exerts forces on the obstacles and the channel embankments, and modifies bed morphology (Campisano et al., 2004; Meurice et al., 2022; Soares-Frazão et al., 2007). This presents a challenge for materials and design engineers in developing fluvial structures that can adapt to extreme flooding scenarios, as well as for calibrating and validating numerical erosive models.

Shallow-flow models are suitable for representing distributed information of the flow evolution in river flood events, usually involving sediment transport and erosive processes. Therefore depth-averaged mathematical approaches have been widely developed for hydro-morpho-dynamic surface flows (Castro-Díaz et al., 2008; Charru, 2006; Devauchelle et al., 2007; Ferreira et al., 2015; Hudson and Sweby, 2003; Yue et al., 2008). Many contributions have been reported for numerical simulation of erosive free surface flows, most of them based on the shallow water hypothesis (Armanini et al., 2009; Ferreira et al., 2009; Fraccarollo et al., 2003; Juez et al., 2014; Martínez-Aranda et al., 2021; Martínez-Aranda et al., 2021). There have been continuous advances in computation, simulation times and performance, together with the development and refinement of robust methods derived from the shallow-flow approach. In this context, it is crucial to be able to validate these models and verify the ability to capture flow phenomena and morphological changes (Canelas et al., 2013; Fernandez-Nieto et al., 2014; Martínez-Aranda et al., 2021; Martínez-Aranda et al., 2021). There have been valuable reported measurement campaigns in this sense (Juez et al., 2017; Lantz et al., 2022; Leal et al., 2008; Martínez-Aranda et al., 2018; Meurice et al., 2022; Soares-Frazao et al., 2012; Soares-Frazão et al., 2007; Spinewine and Zech, 2007). However, the low number of 2D experimental flow measurements, specially in the case of transient erosive flows, highlights the necessity of new contributions and justifies the relevance of the present work.

Image techniques to characterize free surface flows have been developed during last decades (Bento et al., 2022a; Soares-Frazão, 2020). Two-dimensional maps of the water free surface and movable bed surface have been successfully recorded using laser profilommetry, photogrammetry or image surface tracking (Cochard, 2007; Meurice et al., 2022). Recently RGB-D sensor-based recording methods have been developed for measuring free surface of opaque fluid and solid bottom surfaces. The most widely used distance sensors are based on structured light (Kinect-v1, Astra), time of flight (Kinect-v2, Azure, Femto) and stereo vision (Gemini, RealSense) (Berger, 2014; Combes et al., 2011; Huang et al., 2023; Martínez-Aranda et al., 2018; Navas-Montilla et al., 2021; Sarbolandi et al., 2015). These methods provide a non-intrusive, high-resolution approach to

capture bed dynamics and flow interactions with obstacles. Complementary, image techniques for measuring velocity fields, such as PIV or PTV, are usually applied Aleixo et al. (2019, 2011); Muste et al. (2008); Weitbrecht et al. (2002), and even combined with the RGB-D measurements(Martínez-Aranda et al., 2024).

The present study focuses on the experimental characterization of the bed surface changes around rigid structures due to dambreak waves over a dry, erodible sand bed. The Kinect-v1 device (Microsoft, 2010) is used to perform instantaneous measurements of the transient experiments. The applied experimental methodology allows to obtain a 2D maps of the transient water free surface instead of single point measurements at probes. Moreover, 2D maps of the bed surface are captured after the dambreak wave. The main goal is to generate high-quality experimental data for the validation and calibration of 2D numerical hydro-morphological models. These validated models might contribute to gain insight into non-cohesive erosive processes. The paper is structured in the following sections: Section 2 describes the experiment setup; Section 3 is devoted to introduce the surface measurement with the Kinect-v1 device; the resulting dataset is presented in 4, as well as the analysis of its main characteristics; finally conclusions are drawn in 5.

2 Experimental Setup

The experiments were carried out at the Fluid Mechanics Laboratory (Figure 1) of the University of Zaragoza, Spain (Martínez-Aranda et al., 2021, 2019; Navas-Montilla et al., 2021) using a methacrylate rectangular cross section flume 600 cm long and 24 cm wide with no slope in the first 300 cm (Figure 2). The Manning coefficient for the PVC was calibrated to $n = (0.010 \pm 0.002)\ sm^{-1/3}$ in (Martínez-Aranda et al., 2018). It is connected by a pneumatic gate to an upstream reservoir 81 cm wide and 157 cm long. The width of the flume is altered by different PVC elements to form obstacles that can modify the flow configuration.

A central region of length 150 cm, located 100 cm from the upstream reservoir, is filled with a 5 cm thick layer erodible bed composed of non-cohesive sand initially levelled with the channel bed. The sand in the erodible bed is a mixture of two different sizes (see Table 1). Its overall porosity was calculated using the experimental relation $\xi = 0.13 + 0.21 \cdot (d_{50} + 0.002)^{-0.21}$ from Wu (2007), leading to a porosity value of $\xi = 0.34 \pm 0.013$. The transported sediment is collected using five consecutive vertical traps made of PVC. These traps are positioned at the bottom of the sloping downstream channel, 3.25 m from the gate and 1 m beyond the erodible region (Figure 2), where particles settle by gravity. After each experiment, the sand is collected from the traps.

Six geometrical configurations were designed to create a channel narrowing and lateral cavities within the flume. The purpose of these geometries was to generate distinct flow patterns from the impact of a dambreak wave. Different shapes, involving semicircular and rectangular PVC obstacles, were used for the lateral obstacles and piers with circular and ellipsoidal geometries. The choice of these configurations aims to model usual structures in hydraulic engineering, like narrowings (Venturi, Parshall flumes), lateral cavities and bridge piers. All the elements were constructed on PVC plastic material that is rigid and with similar properties to methacrylate.

- **O2 lateral configuration**: Two semicircular columns of radius r=5.5 cm were located opposed on both sides of the channel creating a smooth transition to a narrower section in the flow, with narrowing ratio, $\delta = w_{flume}/w_{narrowing} = 1.87$. The center of the obstacles is separated 160 cm from the gate (Figure 3a).
- **C2 lateral configuration**: Two rectangular columns of dimensions 5.5×11 cm were located opposed on both sides of the channel creating a sharp narrower section in the flow, with $\delta = 1.87$ and located 160 cm after the gate position (Figure 3b).
- **O4 lateral configuration**: Four consecutive semicircular columns of radius $r = 5.5$ cm were located on one side of the channel conforming smooth lateral cavities. They were spaced at 11

cm intervals leaving equal spacing of structure and cavities and conforming widths of 24 cm in the cavities and 18.1 cm in the center of the obstacles. The center of the second obstacle is aligned with the reference point, and therefore separated 160 cm from the gate (Figure 4a).

- **C4 lateral configuration**: Four consecutive rectangular columns of dimensions 5.5×11 cm were located on one side of the channel conforming sharp lateral cavities. They are spaced at 11 cm intervals leaving equal spacing of structure and cavities. This generates changes in the flume width: 24 cm in the cavities and 18.1 cm in the obstacles. The center of the second obstacle is aligned with the reference point, and therefore separated 160 cm from the gate (Figure 4b).
- **P1 central configuration**: A circular obstacle of diameter $r = 3$ cm was located in the middle of the channel emulating a pier in the center of the river. The center of this obstacle is separated 160 cm from the gate (Figure 5a).
- **P2 central configuration**: A rectangular obstacle with rounded laterals of width $d = 3$ cm and length $D = 6.5$ cm was located in the middle of the channel emulating a longer pier in the center of the river. The location of this obstacle is 160 cm from the gate (Figure 5b).

For each geometrical configuration, the same procedure is followed: three consecutive dambreaks are performed without resetting to the uniform bed state. The initial Water Surface Elevation (WSE) for each dambreak is 8 cm of water on a dry bed. The experiment is only continued after the bed is completely dry.

2.1 *Dimensional analysis and experimental scaling*

The dimensional analysis of the case can be useful to scale the case into other modeled situations. The same hydrodynamic behaviour of this experimental setup can be reproduced in bigger cases by preserving some dimensionless numbers that characterize the flow. In particular, we are concerned with the Froude number (Fr) as it regulates the flow dynamics and the transition of regime from subcritical to supercritical flows. For the characteristic dambreak over a dry bed (Castro-Orgaz and Chanson, 2017), the flow transitions from a subcritical state to a supercritical one, traversing through the critical condition of $Fr = 1$ at the gate section. The analytical solution derived from the Ritter model (Castro-Orgaz and Chanson, 2017) for this simplified scenario forecasts a completely supercritical flow in the downstream erosive region, with a value of $\mathrm{Fr}(x = 1\ \mathrm{m};\ t = 1.5\ \mathrm{s}) \approx 2.81$. This order of magnitude is consistent with empirical observations; the front advance velocity estimated from the water surface elevation (WSE) transient measurements in the O2 case yields $v \approx 0.7\ \mathrm{m\ s^{-1}}$. For a water depth of $h \approx 0.01$ m, a value of Fr= 2.16 is ascertained, we can therefore deduce that the Froude number is approximately 2. The friction slope is also considered as a relevant dimensionless parameter. The difficulties for scaling both hydrodynamics and sediment transport phenomena is well documented in the literature (Heller, 2011), given that preserving Froude number to correctly adress the pure hydrodynamics leads to a different scaling on the Reynolds number, this implies that viscouse forces (often important in sediment phenomena, as different grain size, leads to different sediment dynamics). Furthermore, additional scale effects arises in erodible bed experiments because of sediment dynamics, since some bed layer properties, such as cohesion and porosity, change depending on the sediment size. This increases the uncertainty on the scaling process and make it often not realisitic. Therefore, the authors encourage to use the dataset with a careful scaling of all the terms to validate numerical models. However, in a certain range of application, and being aware that scaling Froude number has its limitations regarding transport process, this scale analysis can enlight the modeling.

Preserving the Froude number between the laboratory situation (L) and a larger model situation

(m) requires:

$$\mathrm{Fr} = \frac{u_m}{\sqrt{g h_m}} = \frac{u_L}{\sqrt{g h_L}} \Rightarrow \frac{u_m^2}{u_L^2} = \frac{h_m}{h_L} = \lambda$$

being λ a geometrical scaling factor between the laboratory setup scale and the real model scale. This provides the scaling rule for the velocity:

$$\frac{u_m}{u_L} = \sqrt{\lambda}$$

To enforce roughness coefficient scaling, the uniform steady situation is employed, yielding $S_0 = S_f$. Distances scale with λ, leading to $S_{0,m} = \frac{\partial \lambda z_{b,L}}{\partial \lambda x_L} = S_{0,L}$. This condition necessitates that S_f remains consistent between Lab and model configurations. Expressing S_f via Manning's law and presuming positive velocity yields:

$$S_0 = \frac{n_m^2 u_m^2}{h_m^{4/3}} = \frac{n_L^2 u_L^2}{h_L^{4/3}} \Rightarrow \frac{n_m}{n_L} = \lambda^{1/6}$$

Where S_0 is the channel bed slope and S_f is the friction slope, which are the source terms in the momentum conservation equation.

Finally, for the sediment scale, the Shields number provides the dimensionless version of the shear stress. The bed shear stress can be written in terms of the friction term

$$\tau_b = \rho_w g \frac{n^2 u^2}{h^{1/3}}$$

and, therefore, the Shields number,

$$\theta = \frac{\tau_b}{(\rho_s - \rho_w) g D}$$

when assuming the same sediment density, yields[1]:

$$\frac{n_m^2 u_m^2}{h_m^{1/3} (\frac{\rho_s}{\rho_w} - 1) d_m} = \frac{n_L^2 u_L^2}{h_L^{1/3} (\frac{\rho_s}{\rho_w} - 1) d_L} \Rightarrow \frac{d_m}{d_L} = \lambda$$

In summary, we can scale all the lengths in the model with the λ parameter, and the roughness coefficient with $\lambda^{1/6}$. For example, for comparing the experimental measurements with a real case where the circular pier in P1 case (see Figure 5) has instead a diameter of $d_m = 0.6$ m, we have a $\lambda = 60/3 = 20$. So, the initial height of the dambreak should be of $h_m = \lambda h_L = 1.6$ m, the Manning coefficient should be $n_m = 20^{1/6} \cdot 0.015 = 0.025$ s m$^{-1/3}$, and the size of the particles should be $D_m = 20 \cdot 1$ mm $= 2$ cm. With this scaled parameters the behaviour of the case would be similar to this experimental dataset if the change is purely hydrodynamic and if changes on the sediment size does not significantly affect the soil mechanics properties (as permeability or suction can modify apparent cohesion).

[1]Note that we are scaling the diameter of the sand particles, but we could have also scaled the density of the material for example

3 Measurement Techniques

While traditional methods like PIV and PTV are the gold standard for detailed velocity field analysis, the Kinect offers a complementary approach. Unlike PIV/PTV, which track particles to measure fluid kinematics, the Kinect's strength lies in its ability to measure water surface elevation and bed topography non-intrusively. Therefore, this new technique is not directly comparable to PIV/PTV, as they target distinct physical quantities and require fundamentally different experimental setups—the Kinect needs tinted water, while PIV/PTV requires particle seeding. Compared with traditional methods for surface elevation measurement (gauges, pressure-transducers or ultrasonic sensors), the Kinect presents important advantages, especially in a lab context, by providing spatial maps rather than single-point measurements, all with high resolution.

The Kinect device takes RGB and distance (D-sensor) images independently at 30 Hz sampling rate, projecting an infrared grid of 640x480 pixels. The characteristics of the experimental setup and the position of the Kinect sensor ≈ 80 cm above the PVC bed (Figure 2) results in ~ 1.4 mm of spatial resolution. For the D-sensor sampling, the vertical resolution in the depth measurements is $\Delta z \approx 1.5$ mm for a laboratory setup with kinect sensor 80 cm above the bed (Sarbolandi et al., 2015).

The field of Vision of the Kinect sensor is centered in the sand region (between 1.2 m and 2.0 m, Figure 2), going from, and is used to perform the transient measurements of the water dambreak wave propagation over the movable bed. The Kinect projects an infrared mesh and measures the reflected pattern. This grid has a wavelength of 830 nm (Zennaro et al., 2015) which makes easy to record the solid and reflecting sand material at the bed level. However, for recording the water surface the fluid must be tinted using Titanium Dioxide (TiO_2) that gives water a high reflectance in the IR range without affecting the fluid properties, making it opaque to the kinect sensor.

Each experiment was configured as follows: a flushing wave, generated from a dambreak with an initial height of 8 cm, was released from the 81 cm $\times$ 157 cm upstream reservoir over a dry bed and repeated three times over the gradually eroded bed. The overall experimental procedure followed the methodology outlined in Figure 6.

- *Initial state*: A dry, flat sand bed before water release is measured. A few seconds are recorded and averaged in order to avoid noise and to obtain a homogeneous mesh that can be used as reference map for the case (Figure 7).
- *WSE dambreak flow*: A dambreak of 8 cm is performed, and a transient sequence of 2D maps is recorded with 30 fps for the water surface elevation during the event. The synchronization between Kinect and gate opening is performed using a LED diode visible in the Kinect RGB image. The electrical signal for opening the gate also turns on the LED, so the time stamp of the transient measurements is referenced to this time. This time dependent data is recorded for each of the three consecutive dambreak events (Figure 8a).
- *Final bed state*: After each dambreak and once surface water has disappeared from the bed, the resultant sand pattern is recorded for two seconds and averaged, obtaining the morphological deformation of the sand bed referenced to the initial state (Figure 8b).

The data output produced by the Kinect sensor, recorded at a resolution of 640x840 pixels and approximately 30 fps needs post-processing. This was performed using a combination of `C++, Matlab, Python` and `bash`:

Data processing began with the conversion of raw binary information into **.ply* point clouds. The point clouds are referenced using (X, Y) coordinates, measured in millimeters. The X-axis is aligned with the flume wall, originating at the gate. The Y-axis is perpendicular to the flume walls, originating at the right wall (as viewed from the gate). Each (X, Y) point was associated with a depth value and 3-channel RGB image data. To correct for minor Kinect alignment errors, the point cloud then underwent a plane rotation (Figure 9 if $\alpha > 0.1$, Table 2), and all transient recordings

were referenced to the gate's opening time by using the LED diode. It is worth noting that Z values were adjusted to the initial reference level. By doing this, erosion patterns were associated to negative values while deposition to positive values. Subsequently, the flume geometry was masked to eliminate structural artifacts. A threshold filter was applied, based on the 0.04% lower and higher percentiles, specifically to remove any excessively high points potentially caused by interactions with the experimental structure. To address missing individual points, which could occur due to reflections from the irregular water surface, data gaps were filled using `numpy.nanmean` to calculate the average value of neighboring points. The final processing step involved a convolutional operation to smooth the Z values, applying a zero-mean Gaussian filter. The filter's standard deviation was set to $\sigma = 1.5$ mm, which effectively suppressed high-frequency noise originating from the Kinect sensor within the 2D dataset (Figure 10).

4 Results

4.1 *Validation*

To validate the experimental setup (flume and pneumatic gate) and the measurement technique (Kinect device), we performed a repeatability analysis along with a gate opening calibration. To characterize the gate opening dynamics, the process was recorded using a high-speed camera at 60 frames per second (fps), allowing us to capture the temporal evolution of the gate position with high resolution. From the recorded frames, we extracted the gate displacement over time and computed the corresponding velocity profile (see Figure 11). These measurements provide insight into the mechanical response and inertia of the gate system and can be incorporated into numerical modeling.

In comparison with the Lauber–Hager instantaneous collapse criterion, which assumes a gate removal time of

$$t_c = \sqrt{\frac{2h_0}{g}} \leq 0.1277\,\mathrm{s},$$

our gate opening is within acceptable limits. By excluding the initial 50 ms—during which the gate moves less than 1 cm and can be considered quasi-static—the effective opening time is reduced to under 100 ms, aligning well with the criterion for simulating dambreak-like conditions.

Two independent dambreak experiments were conducted under identical conditions over a uniform rectangular cross-section, fixed bed, both with an initial water height of 8 cm. The time evolution of the Water Surface Elevation (WSE) was analyzed at three distinct sections along the flume (see Figure 12) to compare the results, the values presented correspond to the time evolution of the averaged values along the vertical section.

To provide a quantitative measure of the deviation, the **Mean Absolute Error (MAE)** was calculated at each point. The MAE measures the average magnitude of the errors between the two datasets and is defined as:

$$\mathrm{MAE} = \frac{1}{n}\sum_{i=1}^{n} |y_i - x_i| \tag{1}$$

where y_i and x_i are the paired measurements from the two tests and n is the total number of data points.

The calculated errors are summarized in Table 3. The low MAE values demonstrate a high degree of consistency between the repeated tests, confirming the reliability and precision of the experimental procedure.

4.2 *Experimental dataset*

Each experimental case was analyzed by examining and processing both the transient water surface elevation (WSE) data and the static sand form after each dambreak. These experiments consisted of three sequential dambreak events, or "waves," conducted for each case to investigate the cumulative effect of repeated erosion on the sand bed. The initial bed position in the erodible region was therefore altered for each subsequent dambreak event due to the erosion from the previous run. The primary dataset consists of `*.h5` files (see details in Appendix B), which can be opened in `Python` using the `h5py.File` class of the module for HDF5 files (see the usage example in Appendix A), or the `h5read` function of `Matlab`. Check all the available files in Table 4. All water transient files are organized into separate folders. To reduce noise, the sand bed measurements were averaged over 50 frames obtained from the dry bed recording.

4.3 *Two-dimensional WSE and bed surface maps*

This section presents and discusses maps of the transient water surface and the resulting bedforms after each dam break.

Figure 13 shows the erosion and deposition patterns for configurations O2 (a) and C2 (b) after consecutive dam breaks. In both cases, erosion is observed around the obstacles and in their wakes. Notably, the O2 configuration presents a more marked scour around the obstacles, as well as a clear erosion jet downstream that does not exist in the C2 case. The Figure 14 depicts the bed maps for the embayment configurations, (a) O4 case and (b) C4 case. The resulting bed changes are characterized by significant sediment deposits inside the cavities, which increases with consecutive dambreaks. This deposition pattern is enhanced by the rounded shape of the obstacles, specially in the first cavity upstream. Finally, Figure 15 illustrates the scour patterns for the pier cases, P1 (a) and P2 (b). Both configurations exhibit clear scour around the obstacles and a deposition pattern in their wake. The P2 case seems to reduce the downstream scour and to enhance the deposition in the wake region.

The results show that obstacle geometry significantly influences sediment transport and erosion patterns, demonstrating differences in the subsequent dambreak waves. Cases with multiple consecutive obstacles (C4, O4) exhibit more localized erosion zones with deposit zones in the cavities, whereas central faced obstacles (C2, O2) result in severe symmetrical erosion patterns around the obstacles, presenting heavy erosion in the narrowing. We can observe that while the magnitude of the erosion can slightly increase over consecutive dambreak waves, the changes diminish for the second and third waves (Figures 13, 15). As studied by Lu et al. (2013), an equilibrium profile for the scouring process is achieved in a steady flow. In these experiments, we can observe a quasi-equilibrium state. This is likely because the flow reached a quasi-steady state during the long dambreak, before the reservoir emptied, allowing the bed to achieve a very stable condition by the end of the first dambreak (Lu et al., 2013). This stability produced a higher resistance to erosion in subsequent events.

Additionally, the 2D maps of WSE for each dambreak experiment can be extracted from the transient data at the desired times. Figure 16 presents the WSE evolution for (a) the O2 and (b) the C2 narrowing configurations at four different times. Figure 17 shows WSE maps at four different times for (a) the O4 and (b) the P1 configurations. These maps illustrate the propagation of the wave and its interaction with the various obstacles. For the narrowing cases, a high column of water appears around both lateral obstacles after the wave front arrival (see Figure 16-3rd row), that evolves and creates a transient jump upstream the narrowing (see Figure 16-4th row). The wake produced by the O4 and P1 configurations produces elevations of the WSE around the obstacles.

4.4 *Profile and probes analysis*

The 2D grid structure of the data facilitates the straightforward analysis of bed elevation and WSE changes along arbitrary transects within the domain. A transient jump is generated upstream the obstacles in both the O2 and C2 cases (see Figure 16). Figure 18 show the longitudinal profile of WSE along the centerline at four different times. In the C2 case, the effect of the lateral obstacle merges within the upstream region, creating a much higher WSE peak. This difference in hydrodynamic behavior leads to modifications of the wave shapes observed in the profiles (Figure 18), where a water height of almost 9 cm is achieved in (b) the C2 case .

Figure 19 plots the transversal profiles of the bed level at the cavities location after each dambreak experiment, for the first cavity (a, b) and last cavity (c, d). In the C4 lateral cavity configuration, the resulting morphodynamic changes are evident both inside and outside the cavities. For the O4 case, erosion is most pronounced in the constricted region, reaching its maximum near the obstacles. Downstream of the obstacles, a distinct pattern emerges, with scour in the center of the channel and deposition along the lateral walls. Profiles show that the cavities retain sediment, with deposition depths ranging from 1 to 2 cm. These structures, therefore, function as sediment traps, and their potential application for river restoration is a subject of ongoing study within the ecohydrology community (Juez et al., 2018).

Figure 20 shows the transversal profiles of the bed level at different sections for the (left) P1 case and (right) P2 case. The experimental results show an important scouring process around the pier. Figure 5-third row shows the 2D map of erosion/deposition pattern after third dambreak for (a) P1 case and (b) P2 case. It is worth noting that, despite our experiments deal with transient erosive flows, the obtained results show a good agreement with steady experiments carried out in piers scouring, with a marked erosion upstream the pier and deposition at the wake region downstream (Bento et al., 2022b; Breusers and Raudkivi, 2020; Lu et al., 2013; Melville and Raudkivi, 1996). Furthermore, Figure 21 depicts the longitudinal bed profile along the channel centerline for (a) P1 case and (b) P2 case. For a more quantitative comparison, we use the simplified approach from Breusers and Raudkivi (2020), which suggests a maximum scour depth of $y_s/b = 1.5$ at the upstream region of cylindrical piers. In our case, the pier diameter is $b = 3$ cm, leading to a theoretical $y_s = 4.5$ cm scour depth. Our experiment shows a scouring depth of $y_s \sim 2$ cm. This value is expectedly lower because our experiments use transient dambreak waves and the maximum erodible layer is 5 cm thick due to the setup.

Also, it is possible to plot data versus time during each dambreak event. Selecting the coordinates of interest allows to extract the water surface elevation (WSE) for each time. Some results can be observed in Figure 22 for the O2 configuration and in Figure 23 for the C2 case. It can be observed how the front arriving time varies depending on the point. It can also be noticed that WSE for the first dambreak wave shows a more uniform and smooth evolution, while 2nd and 3rd waves have more peaks and a more ondulatory tendency. This is possibly due to the change in the bed level, creating an irregular topography that lead to surface waves (Davies and Heathershaw, 1984). It is important to remark that we are measuring the water surface elevation referenced to the initial bed level (sand0) and not the water column; for this reason we can observe negatives values before the 2nd and 3rd waves are released (Figures 22, 23).

Table 5 presents a quantitative comparison between the initial theoretical sediment mass and the measured mass at different stages: the initial state (`sand0`) and after each of three successive dambreaks (`sand1` to `sand3`). The analysis focuses on the O2 and C2 experiments within a Region of Interest (ROI), as depicted in Figure 24. The ROI is defined as a rectangle with x-limits from 1400 to 1600 mm and y-limits from 68 to 172 mm. This positioning avoids including parts of the obstacles and focuses the analysis on the region between them.

The results for the initial state (`sand0`) show excellent agreement with the theoretical mass, which was calculated based on a rectangular prism of sand with dimensions of $200 \times 104 \times 50$ mm. However, successive dambreak events reveal that the final measured mass is consistently lower,

indicating sediment erosion during the process. This highlights the inherent scour in the region between the obstacles. Notably, the rectangular configuration (C2) repeatedly shows higher mass differences over the three dambreaks, being on average 31.0% higher.

5 Conclusions

The presented set of experiments is of great relevance due to the lack of 2D measurements in free surface transient flows, specifically in those with movable bed and erosion phenomena. The use of distance sensors, in this case Kinect v1, allows for non intrusive measurements of the WSE, recording a high quality map for each time stamp at 30 fps. The sand level after each dambreak is also correctly captured once the flume bottom is dried.

The study demonstrates that obstacle setup plays a crucial role in the flow characteristics and erosion patterns in shallow water dambreak scenarios, narrowing situations, lateral cavities and central obstacles have been studied. The shape of the obstacles (circular, square) also have important effects in the magnitude and pattern of the scouring process. Key findings include:

- Multiple obstacles on one side (C4, O4) create local seiches waves and recirculation zones, leading to deposition patterns inside the cavities. Central obstacles (P1, P2) generate symmetrical flow patterns, highly increasing the wse in the front of the obstacle, causing important erosion around the piers. This eroded material is deposited in the central part of the wake after the obstacle, probably due to the lower flow velocity. The narrowing in C2/O2, works as a barrier, slowing the water upstream the obstacles, increasing water column depth (see Figure 16), which significantly increases the erosion.
- Regarding the shape of the obstacles, the rectangular obstacles show higher influence in the flow, increasing water depth and vortex shedding inside the cavities, what can decrease the velocity, affecting erosion patterns. The round obstacles, given their smooth surface, present smaller re-circulation patterns in the flow as shown in Figure 16. This makes possible that rounded obstacles (O2,O4) present deeper scouring patterns around the obstacles, even creating erosion regions or not depending on the shape (see scouring patterns in Figure 14).
- Post-processing methodology, including plane rotation, percent thresholding or Gaussian filtering, effectively reduces noise while preserving the essential morphological features of the eroded bed, proving itself reasonable treatments for filtering experimental data. The important availability of libraries and modules for signals analysis highly eases the process.

The public data, the structured grid, as well as the chosen format `*.h5`, make easy to work and use the data with the most common developer software such as `python`, `R` or `matlab`; being direct the extraction of profiles and observation points.

The findings suggest a valuable hybrid approach for future research in experimental fluid dynamics. While our study focuses on dambreak scenarios, the synergy between the Kinect and techniques like PIV or PTV extends to a wide range of transient erosive flows with structure interaction. The non-intrusive nature of the image analysis techniques, which provides spatial distributed maps instead of local measurements, is a significant advantage, given the high resolution, low cost and non intrusivity. This holds considerable promise for a wide range of laboratory hydraulic applications related not only to sediment transport phenomena, but also surface transport, complex rehological flows, and irregular topography/obstacle effect on the flow in both transient and steady scenarios at lab scale.

Funding

This work was supported by grant PID2022-137334NB-I00 funded by MCIN/AEI/10.13039/501100011033. This work was partially funded by the Aragón Government, DGA (Spain) , through the Fondo Europeo de Desarrollo Regional, FEDER.

Supplemental data

The presented dataset with test cases for O2, C2, O4, C4, P1 and P2 in HDF5 format can be found at the Zenodo repository `https://doi.org/10.5281/zenodo.15601711`.

Notation

n = Manning coefficient (s m$^{-1/3}$)
δ = Narrowing ratio (dimensionless)
$[\cdot]_m$ = Quantities from the modeled situation
$[\cdot]_L$ = Quantities from the laboratory experiment
λ = Longitude ratio parameter (dimensionless)
S_0 = Flume slope (dimensionless)
S_f = Friction slope (dimensionless)
Fr = Froude number, relates inertial and gravity forces (dimensionless)
τ_b = bed shear stress (Pa)
θ = Shields number (dimensionless)
α = Rotation angle applied to the dataset

References

Aleixo, R., Carvalho, E., Lima, M., and Ferreira, R. (2019). Piv-ptv measurements of water and sediment flows. In *HydroSenSoft, International Symposium and Exhibition on Hydro-Environment Sensors and Software*.

Aleixo, R., Soares-Frazão, S., and Zech, Y. (2011). Velocity-field measurements in a dam-break flow using a ptv voronoï imaging technique. *Experiments in Fluids*, 50(6):1633–1649.

Armanini, A., Fraccarollo, L., and Rosatti, G. (2009). Two-dimensional simulation of debris flows in erodible channels. *Computers & Geosciences*, 35(5):993 – 1006.

Bento, A. M., Couto, L., Viseu, T., and Pêgo, J. P. (2022a). Image-based techniques for the advanced characterization of scour around bridge piers in laboratory. *Journal of Hydraulic Engineering*, 148(6):06022004.

Bento, A. M., Couto, L., Viseu, T., and Pêgo, J. P. (2022b). Image-based techniques for the advanced characterization of scour around bridge piers in laboratory. *Journal of Hydraulic Engineering*, 148(6):06022004.

Berger, K. (2014). A state of the art report on multiple rgb-d sensor research and on publicly available rgb-d datasets. *Computer Vision and Machine Learning with RGB-D Sensors*, pages 27–44.

Breusers, H. and Raudkivi, A. (2020). *Scouring: hydraulic structures design manual series, vol. 2*. Crc Press.

Campisano, A., Creaco, E., and Modica, C. (2004). Experimental and numerical analysis of the scouring effects of flushing waves on sediment deposits. *Journal of Hydrology*, 299(3-4):324–334.

Canelas, R., Murillo, J., and Ferreira, R. M. (2013). Two-dimensional depth-averaged modelling of dam-break flows over mobile beds. *Journal of Hydraulic Research*, 51(4):392–407.

Cao, Z., Pender, G., Wallis, S., and Carling, P. (2004). Computational dam-break hydraulics over erodible sediment bed. *Journal of hydraulic engineering*, 130(7):689–703.

Capart, H., Spinewine, B., Young, D., Zech, Y., Brooks, G., Leclerc, M., and Secretan, Y. (2007). The 1996 lake ha! ha! breakout flood, québec: Test data for geomorphic flood routing methods. *Journal of Hydraulic Research*, 45(sup1):97–109.

Castro-Díaz, M., Fernández-Nieto, E., and Ferreiro, A. (2008). Sediment transport models in shallow water equations and numerical approach by high order finite volume methods. *Computers & Fluids*, 37(3):299 – 316.

Castro-Orgaz, O. and Chanson, H. (2017). Ritter's dry-bed dam-break flows: Positive and negative wave dynamics. *Environmental Fluid Mechanics*, 17(4):665–694.

Charru, F. (2006). Selection of the ripple length on a granular bed sheared by a liquid flow. *Physics of Fluids*, 18(12):121508.

Cochard, S. (2007). *Measurements of time-dependent free-surface viscoplastic flows down steep slopes*. PhD thesis, EPFL, Lausanne.

Combes, B., Guibert, A., Mémin, E., and Heitz., D. (2011). Free-surface flows from kinect: Feasibility and limits. Technical Report hal-00676338, FVR2011, Poitiers, France.

Davies, A. and Heathershaw, A. (1984). Surface-wave propagation over sinusoidally varying topography. *Journal of Fluid Mechanics*, 144:419–443.

Devauchelle, O., Josserand, C., Lagrée, P.-Y., and Zaleski, S. (2007). Morphodynamic modeling of erodible laminar channels. *Physical Review E*, 76:056318.

Fernandez-Nieto, E. D., Lucas, C., de Luna, T. M., and Cordier, S. (2014). On the influence of the thickness of the sediment moving layer in the definition of the bedload transport formula in exner systems. *Computers & Fluids*, 91:87–106.

Ferreira, R. M., Hassan, M. A., and Ferrer-Boix, C. (2015). Principles of bedload transport of non-cohesive sediment in open-channels. In *Rivers–Physical, Fluvial and Environmental Processes*, pages 323–372. Springer.

Ferreira, R. M., Leal, J., and Cardoso, A. (2005). Mathematical modeling of the morphodynamic aspects of the 1996 flood in the ha! ha! river. In *31st IAHR Congress 2005: Water Engineering for the Future, Choices and Challenges*, pages 3434–3445. Korea Water Resources Association.

Ferreira, R. M. L., Franca, M. J., Leal, J. G. A. B., and Cardoso, A. H. (2009). Mathematical modelling of shallow flows: Closure models drawn from grain-scale mechanics of sediment transport and flow hydrodynamicsthis paper is one of a selection of papers in this special issue in honour of professor m. selim yalin (1925–2007). *Canadian Journal of Civil Engineering*, 36(10):1605–1621.

Fraccarollo, L., Capart, H., and Zech, Y. (2003). A godunov method for the computation of erosional shallow water transients. *International journal for numerical methods in fluids*, 41(9):951–976.

Goutière, L., Soares-Frazão, S., Savary, C., Laraichi, T., and Zech, Y. (2008). One-Dimensional model for transient flows involving bed-load sediment transport and changes in flow regimes. *Journal of Hydraulic Engineering*, 134(6):726–735.

Heller, V. (2011). Scale effects in physical hydraulic engineering models. *Journal of Hydraulic Research*, 49(3):293–306.

Huang, K., Wu, X., and Lin, Z. (2023). An advanced laboratorial measurement technique of scour topography based on the fusion method for 3d reconstruction. *Journal of Ocean Engineering and Science*.

Hudson, J. and Sweby, P. K. (2003). Formulations for numerically approximating hyperbolic systems governing sediment transport. *Journal of Scientific Computing*, 19:225–252.

Juez, C., Murillo, J., and García-Navarro, P. (2014). A 2d weakly-coupled and efficient numerical model for transient shallow flow and movable bed. *Advances in Water Resources*, 71:93–109.

Juez, C., Soares-Frazao, S., Murillo, J., and García-Navarro, P. (2017). Experimental and numerical simulation of bed load transport over steep slopes. *Journal of Hydraulic Research*, 55(4):455–469.

Juez, C., Thalmann, M., Schleiss, A., and Franca, M. (2018). Morphological resilience to flow fluctuations of fine sediment deposits in bank lateral cavities. *Advances in Water Resources*, 115:44–59.

Lantz, W. D., Crookston, B. M., and Palermo, M. (2022). Evolution of local scour downstream of type a pk weir in non-cohesive sediments. *Journal of Hydrology and Hydromechanics*, 70(1):103–113.

Leal, J. B., Ferreira, R. M. L., and Cardoso, A. H. (2008). Experimental dam-break waves profile analysis: horizontal mobile bed. In *River Flow, Vol. 2*.

Liu, W., Wang, B., Chen, Y., Wu, C., and Liu, X. (2018). Assessing the analytical solution of one-dimensional gravity wave model equations using dam-break experimental measurements. *Water*, 10(9):1261.

Lu, J.-Y., Hong, J.-H., Chang, K.-P., and Lu, T.-F. (2013). Evolution of scouring process downstream of grade-control structures under steady and unsteady flows. *Hydrological Processes*, 27:2699 – 2709.

Martínez-Aranda, S., Fernández-Pato, J., Caviedes-Voullième, D., García-Palacín, I., and García-Navarro, P. (2018). Towards transient experimental water surfaces: A new benchmark dataset for 2d shallow water solvers. *Advances in water resources*, 121:130–149.

Martínez-Aranda, S., García-Palacín, I., and García-Navarro, P. (2024). Free surface velocity measurement in highly-transient viscoplastic flows: combining NIR surface detection and PIV techniques. In *Proceedings of 8th IAHR Europe Congress*, National and international Meetings RNI 116, pages 427–434, 4-7 June, Lisbon, Portugal. LNEC.

Martínez-Aranda, S., Meurice, R., Soares-Frazão, S., and García-Navarro, P. (2021). Comparative analysis of hllc-and roe-based models for the simulation of a dam-break flow in an erodible channel with a 90 bend. *Water*, 13(13):1840.

Martínez-Aranda, S., Murillo, J., and García-Navarro, P. (2021). Comparison of new efficient 2d models for the simulation of bedload transport using the augmented roe approach. *Advances in Water Resources*, 153:103931.

Martínez-Aranda, S., Navas-Montilla, A., García-Palacín, I., and García-Navarro, P. (2019). 2d non-intrusive measurements of dam-break waves in channels with movable bed and width variations. In *Geophysical Research Abstracts*, volume 21.

Martínez-Aranda, S., Murillo, J., and García-Navarro, P. (2019). A 1d numerical model for the simulation of unsteady and highly erosive flows in rivers. *Computers Fluids*, 181:8–34.

Melville, B. W. and Raudkivi, A. J. (1996). Effects of foundation geometry on bridge pier scour. *Journal of Hydraulic Engineering*, 122(4):203–209.

Meurice, R., Martínez-Aranda, S., Ebrahimi, M., García-Navarro, P., and Soares-Frazão, S. (2022). Laser profilometry to measure the bed evolution in a dam-break flow. *Journal of Hydraulic Research*, 60(5):725–737.

Muste, M., Fujita, I., and Hauet, A. (2008). Large-scale particle image velocimetry for measurements in riverine environments. *Water Resources Research*, 44(4).

Navas-Montilla, A., Martínez-Aranda, S., Lozano, A., García-Palacín, I., and García-Navarro, P. (2021). 2d experiments and numerical simulation of the oscillatory shallow flow in an open channel lateral cavity. *Advances in Water Resources*, 148:103836.

Rosatti, G. and Begnudelli, L. (2010). The riemann problem for the one-dimensional, free-surface shallow water equations with a bed step: theoretical analysis and numerical simulations. *Journal of Computational Physics*, 229(3):760–787.

Sarbolandi, H., Lefloch, D., and Kolb, A. (2015). Kinect range sensing: Structured-light versus time-of-flight kinect. *Computer Vision and Image Understanding*, 139:1–20.

Segovia-Burillo, A., Martínez-Aranda, S., Morales-Hernández, M., Fernández-Pato, J., and García-

Navarro, P. (2025). Kinect sediment lab: experimental measurements of bed evolution for 2d dam-break. Zenodo. [Data set].

Soares-Frazao, S., Canelas, R., Cao, Z., Cea, L., Chaudhry, H. M., Die Moran, A., El Kadi, K., Ferreira, R., Cadórniga, I. F., Gonzalez-Ramirez, N., et al. (2012). Dam-break flows over mobile beds: experiments and benchmark tests for numerical models. *Journal of Hydraulic Research*, 50(4):364–375.

Soares-Frazão, S., Le Grelle, N., Spinewine, B., and Zech, Y. (2007). Dam-break induced morphological changes in a channel with uniform sediments: measurements by a laser-sheet imaging technique. *Journal of Hydraulic Research*, 45:87–95.

Soares-Frazão, S. (2020). Review of imaging-based measurement techniques for free surface flows involving sediment transport and morphological changes. *Journal of Hydroinformatics*, 22:958 – 971.

Spinewine, B. and Zech, Y. (2007). Small-scale laboratory dam-break waves on movable beds. *Journal of Hydraulic Research*, 45(sup1):73–86.

Teraguchi, H., Nakagawa, H., Kawaike, K., Yasuyuki, B., and Zhang, H. (2011). Effects of hydraulic structures on river morphological processes. *International Journal of Sediment Research*, 26(3):283–303.

Weitbrecht, V., Kühn, G., and Jirka, G. (2002). Large scale piv-measurements at the surface of shallow water flows. *Flow Measurement and Instrumentation*, 13(5):237–245.

Wu, W. (2007). *Computational River Dynamics*. NetLibrary, Inc. CRC Press.

Wu, W. and Wang, S. S. (2007). One-dimensional modeling of dam-break flow over movable beds. *Journal of hydraulic engineering*, 133(1):48–58.

Yochum, S. E., Goertz, L. A., and Jones, P. H. (2008). Case study of the big bay dam failure: Accuracy and comparison of breach predictions. *Journal of Hydraulic Engineering*, 134(9):1285–1293.

Yue, Z., Cao, Z., Li, X., and Che, T. (2008). Two-dimensional coupled mathematical modeling of fluvial processes with intense sediment transport and rapid bed evolution. *Science China-physics Mechanics Astronomy*, 51:1427 – 1438.

Zech, Y., Soares-Frazão, S., Spinewine, B., , and Le Grelle, N. (2008). Dam-break induced sediment movement: Experimental approaches and numerical modelling. *Journal of Hydraulic research*, 46(2):176–190.

Zennaro, S., Munaro, M., Milani, S., Zanuttigh, P., Bernardi, A., Ghidoni, S., and Menegatti, E. (2015). Performance evaluation of the 1st and 2nd generation kinect for multimedia applications. In *2015 IEEE International Conference on Multimedia and Expo (ICME)*, pages 1–6. IEEE.

Appendix A. Computer Code Availability

A simple script for working with the dataset is provided at `https://doi.org/10.5281/zenodo.15601711` (Segovia-Burillo et al., 2025). The accompanying `requirements.txt` file allows users to create an identical Python environment, ensuring reproducibility and correct usage of the dataset.

Appendix B. Dataset Description

The dataset used in this study is organized into several HDF5 files and folders, structured as follows:

- `offset.h5`: This file contains the initial reference data for the experimental setup.
  - `"gX"`, `"gY"`: Arrays representing the X and Y grid coordinates in millimeters.
  - `"D_offset[mm]"`: A 2D map of the initial sand bed depth relative to the channel bottom. This serves as the primary vertical datum.
  - `"IMG_offset"`: An RGB image showing the initial, undisturbed state of the sand bed.
  - `"mask"`: A binary mask that delineates the sand bed region, with a value of zero outside this area.
- `sand0.h5`: This file establishes the zero-elevation reference for the mobile bed before any dambreak events.
  - `"gX"`, `"gY"`: Grid coordinates, consistent with `offset.h5`.
  - `"Dsand0[mm]"`: A 2D map of zero values, representing the baseline from which subsequent bed changes are measured.
- `sandN.h5`: A series of files (where N is the event number) documenting the cumulative bed topography after each dambreak event.
  - `"gX"`, `"gY"`: Grid coordinates.
  - `"DsandN[mm]"`: A 2D map of the bed elevation after the N-th event, showing the net change from the initial state (see Figure 13).
- `waterN_h5/`: A series of folders (where N is the event number), each containing time-stamped files that capture the transient water surface elevation (WSE) during a dambreak event.
  - `"gX"`, `"gY"`: Grid coordinates.
  - `"wse[mm]"`: The water surface elevation, measured in millimeters, with respect to the initial bed level defined in `offset.h5`.
  - `"time_stamp[s]"`: An attribute within each file indicating the time in seconds from the start of the event.

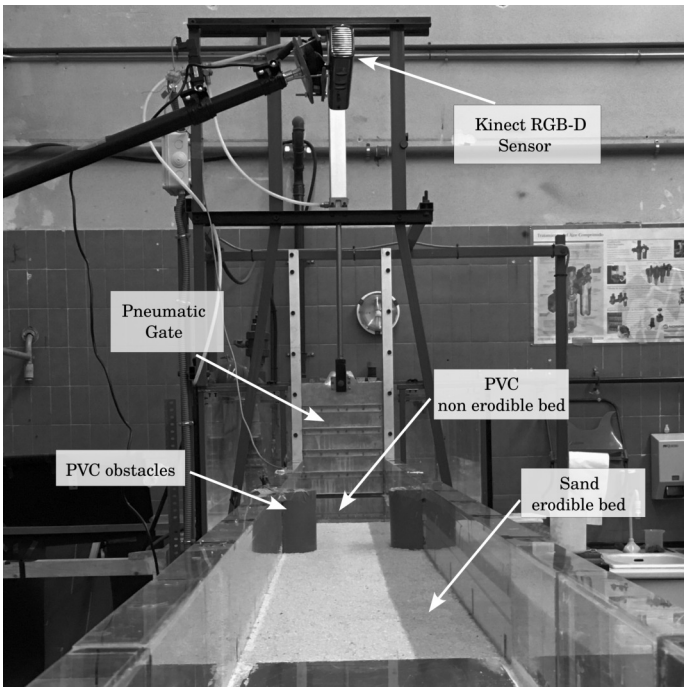

Figure 1 The experimental setup in the Fluid Mechanics laboratory at the University of Zaragoza, showing the main components: the flume, the pneumatic dam-release system, and the Kinect sensor.

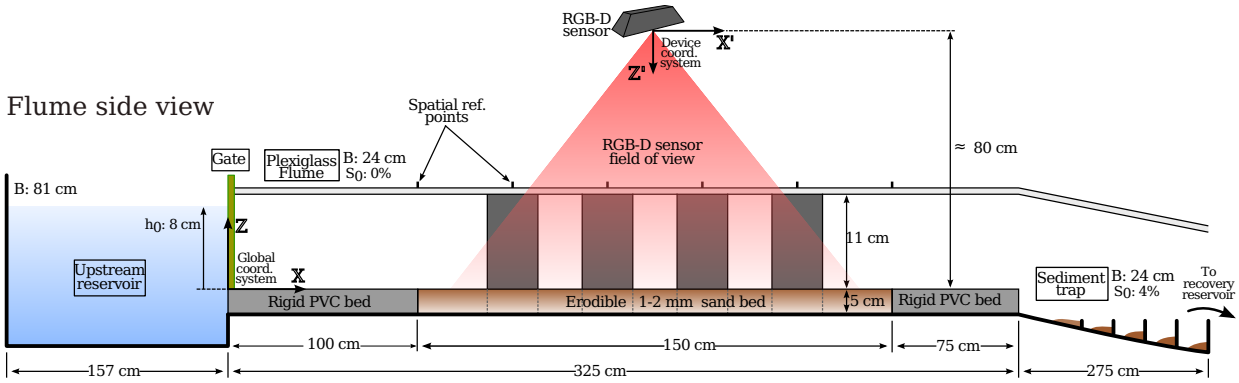

Figure 2 Schematic of the experimental flume (lateral view) showing the main components and key dimensions. The diagram includes the positions of the reservoir, the dam gate, the erodible bed section, the Kinect sensor, and the sediment traps.

Table 1 Erodible bed composition.

Material	Diameter [mm]	Density [kg/m^3]	Fraction	Manning [s m$^{-1/3}$]
Coarse sand	1.3	2650	50%	0.0157
Fine sand	0.7	2650	50%	0.0141

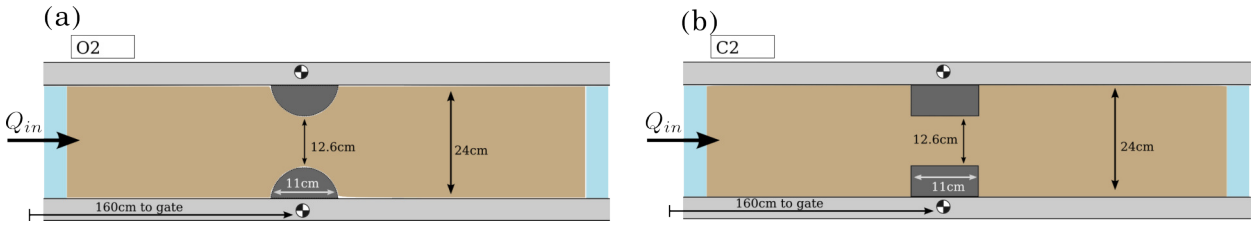

Figure 3 Plan view schematics of the two narrowing configurations tested: (a) Configuration O2, with two circular lateral obstacles, and (b) Configuration C2, with two rectangular lateral obstacles.

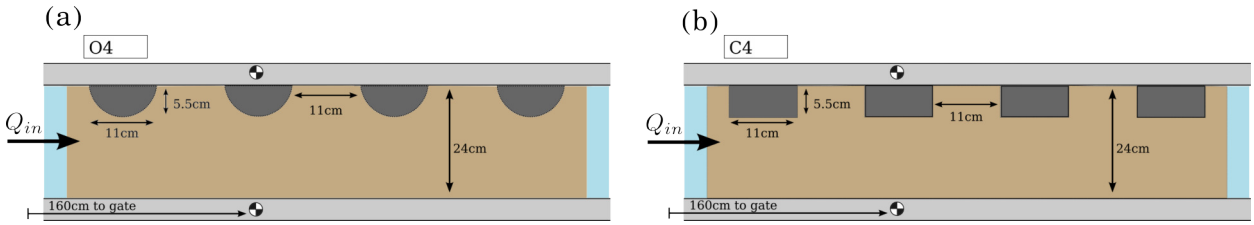

Figure 4 Plan view schematics of the two lateral embayment configurations tested: (a) Configuration O4, featuring rounded/circular embayments, and (b) Configuration C4, featuring rectangular embayments.

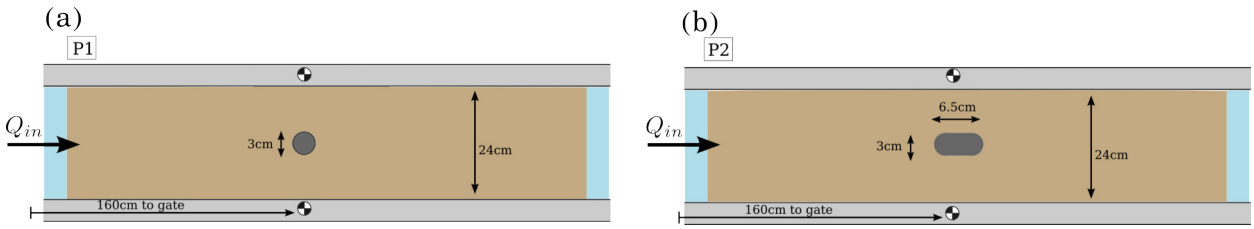

Figure 5 Plan view schematics of the flume showing the two single-pier configurations. (a) The P1 configuration, featuring a single cylindrical pier on the flume centerline. (b) The P2 configuration, featuring a single rounded rectangle pier on the flume centerline. Flow is from left to right in both diagrams.

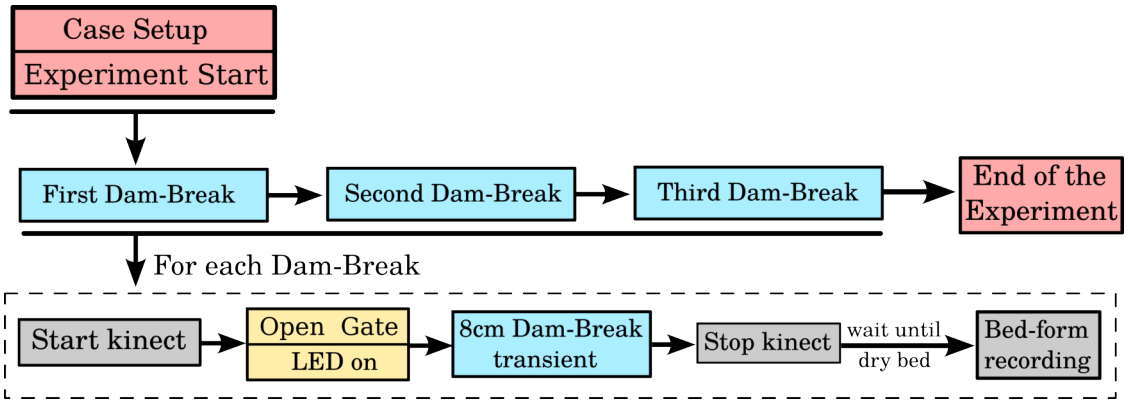

Figure 6 Diagram of the experimental workflow. The overall experiment consists of three consecutive dam breaks. The detailed process for each individual dam break, shown in the dashed box, includes starting the Kinect sensor, opening the gate, capturing the 8 cm dam-break transient, stopping the Kinect, waiting for the bed to dry, and finally recording the resulting bedform.

Table 2 Original rotation (plane angle) of each dataset.

Case	Plane Angle (α, degrees)
C2	0.373
C4	0.325
O2	0.652
O4	0.319
P1	0.393
P2	0.120

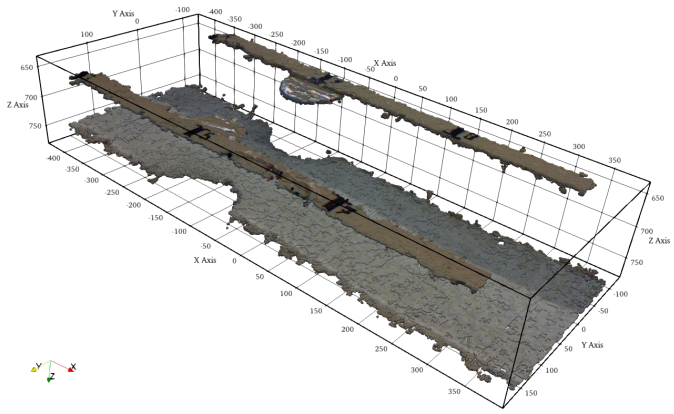

Figure 7 Kinect raw 3D point cloud with RGB color in the Kinect local reference system for offset O2 case.

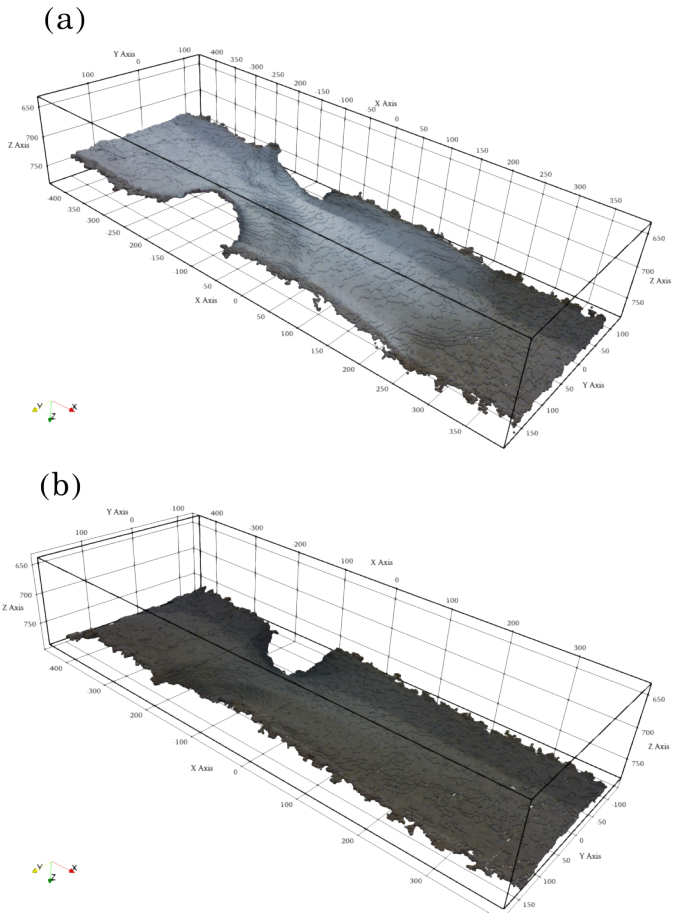

Figure 8 Kinect raw 3D point cloud with RGB color in the Kinect local reference system for water transient (a) and bed-form after first Dam-Break (b) in the O2 case.

Table 3 Mean Absolute Error (MAE) between two repeated experiments at three measurement points.

Measurement Point	**MAE (mm)**
Point 1	1.1163
Point 2	1.0068
Point 3	0.8779

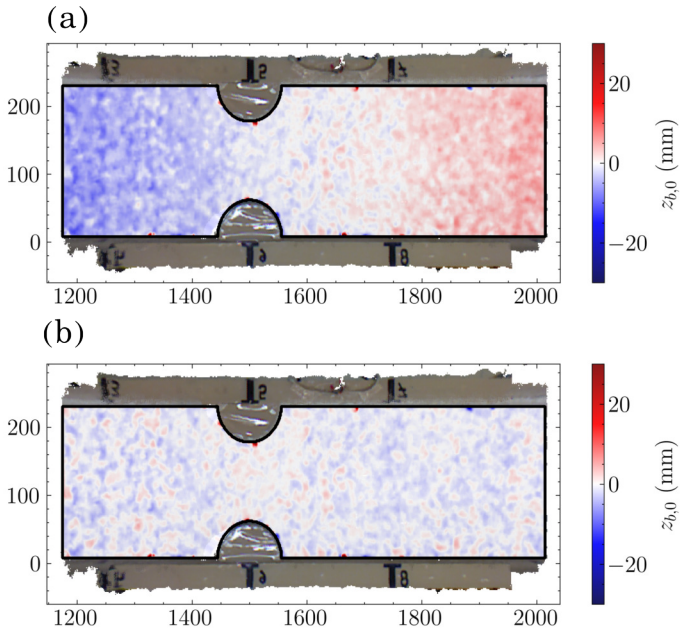

Figure 9 Post-processing plane rotation for reducing kinect missalignements, technique applied to bedform date in (a) sand before rotation, and (b) after processing.

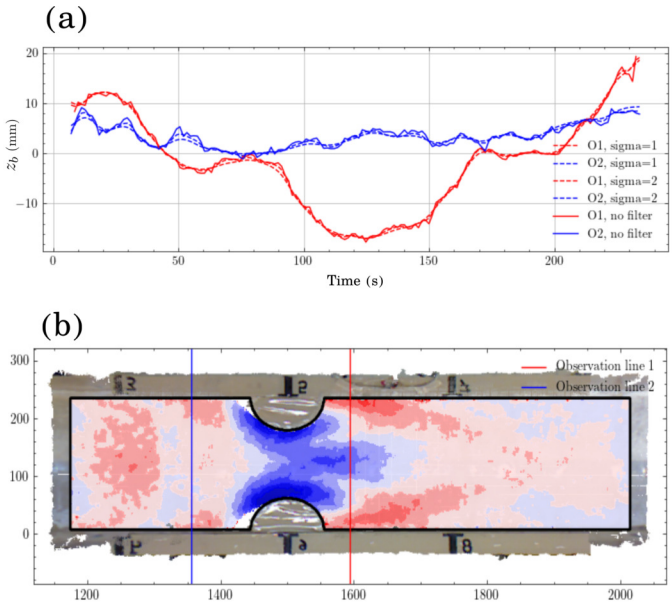

Figure 10 Post-processing noise reduction using a gaussian filter with $\sigma = 1mm$ and $\sigma = 2mm$, reducing inherent kinect fluctuations.

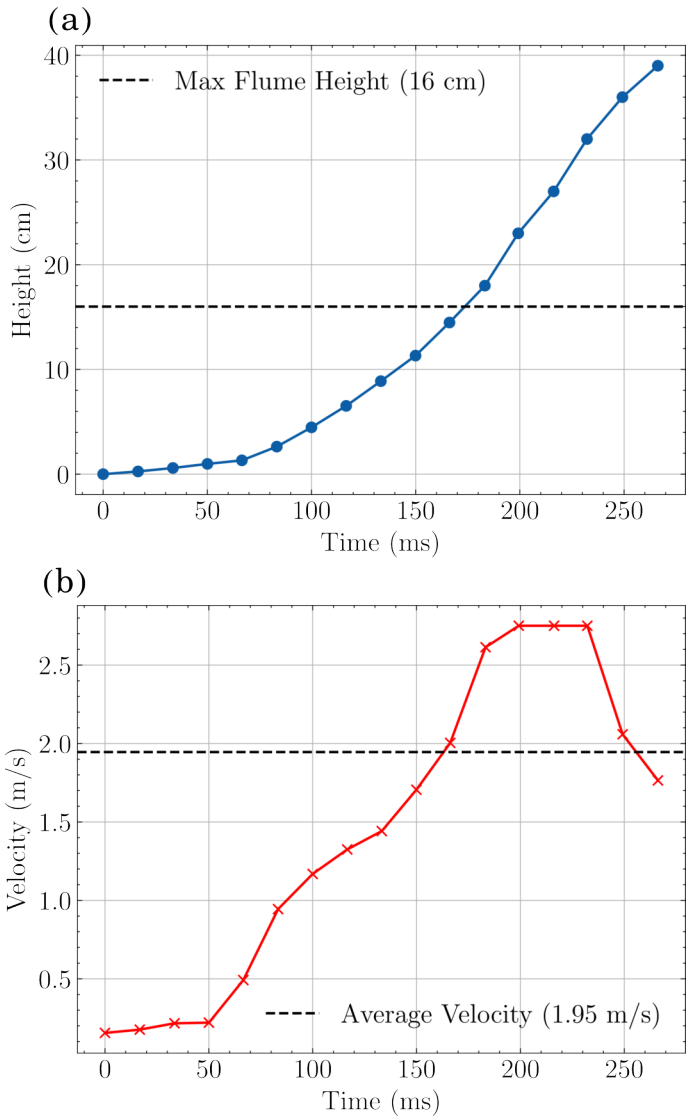

Figure 11 (a) Gate height evolution and (b) velocity profiles obtained from a 60 fps video recording. The horizontal lines represent the flume height (a) and the mean velocity (b), which was calculated by excluding the first and last frames of the opening.

Table 4 Table with all the available data (file/folder names).

Case	Material	Wave 1	Wave 2	Wave 3
O2	Sand	`sand1.h5`	`sand2.h5`	`sand3.h5`
	Water	`water1_h5/`	`water2_h5/`	`water3_h5/`
O4	Sand	`sand1.h5`	`sand2.h5`	`sand3.h5`
	Water	`water1_h5/`	`water2_h5/`	`water3_h5/`
C2	Sand	`sand1.h5`	`sand2.h5`	`sand3.h5`
	Water	`water1_h5/`	`water2_h5/`	`water3_h5/`
C4	Sand	`sand1.h5`	`sand2.h5`	`sand3.h5`
	Water	`water1_h5/`	`water2_h5/`	`water3_h5/`
P1	Sand	`sand1.h5`	`sand2.h5`	`sand3.h5`
	Water	`water1_h5/`	`water2_h5/`	`water3_h5/`
P2	Sand	`sand1.h5`	`sand2.h5`	`sand3.h5`
	Water	`water1_h5/`	`water2_h5/`	`water3_h5/`

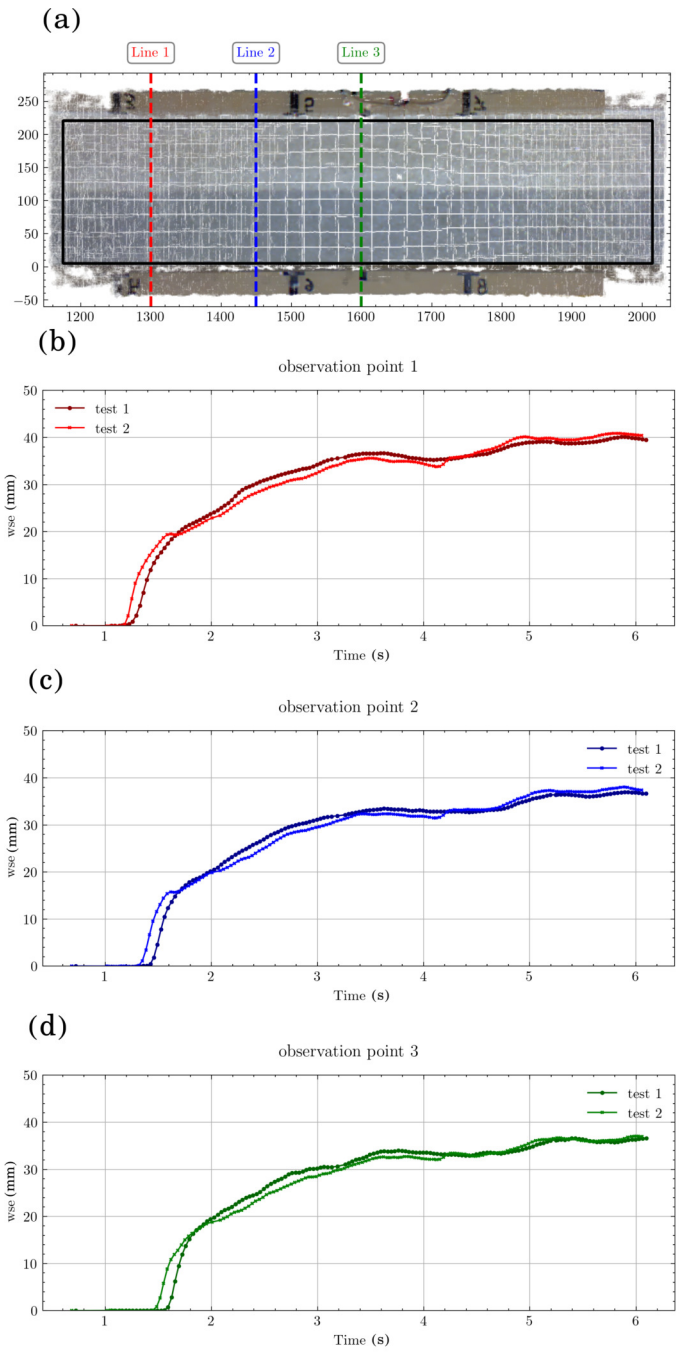

Figure 12 Time evolution sections analysis for the validation case. (a) Observation line locations. (b-d) Water Surface Elevation (WSE) at sections 1, 2, and 3, respectively.

Table 5 Measured sediment mass and difference from the theoretical value of 2.7481 kg.

Measurement	**O2 Mass (kg)**	**O2 Diff. (kg)**	**C2 Mass (kg)**	**C2 Diff. (kg)**
sand0	2.7483	0.0001	2.7478	-0.0003
sand1	2.1023	-0.6458	2.0819	-0.6663
sand2	2.1267	-0.6215	1.8799	-0.8683
sand3	2.2196	-0.5285	1.9541	-0.7940

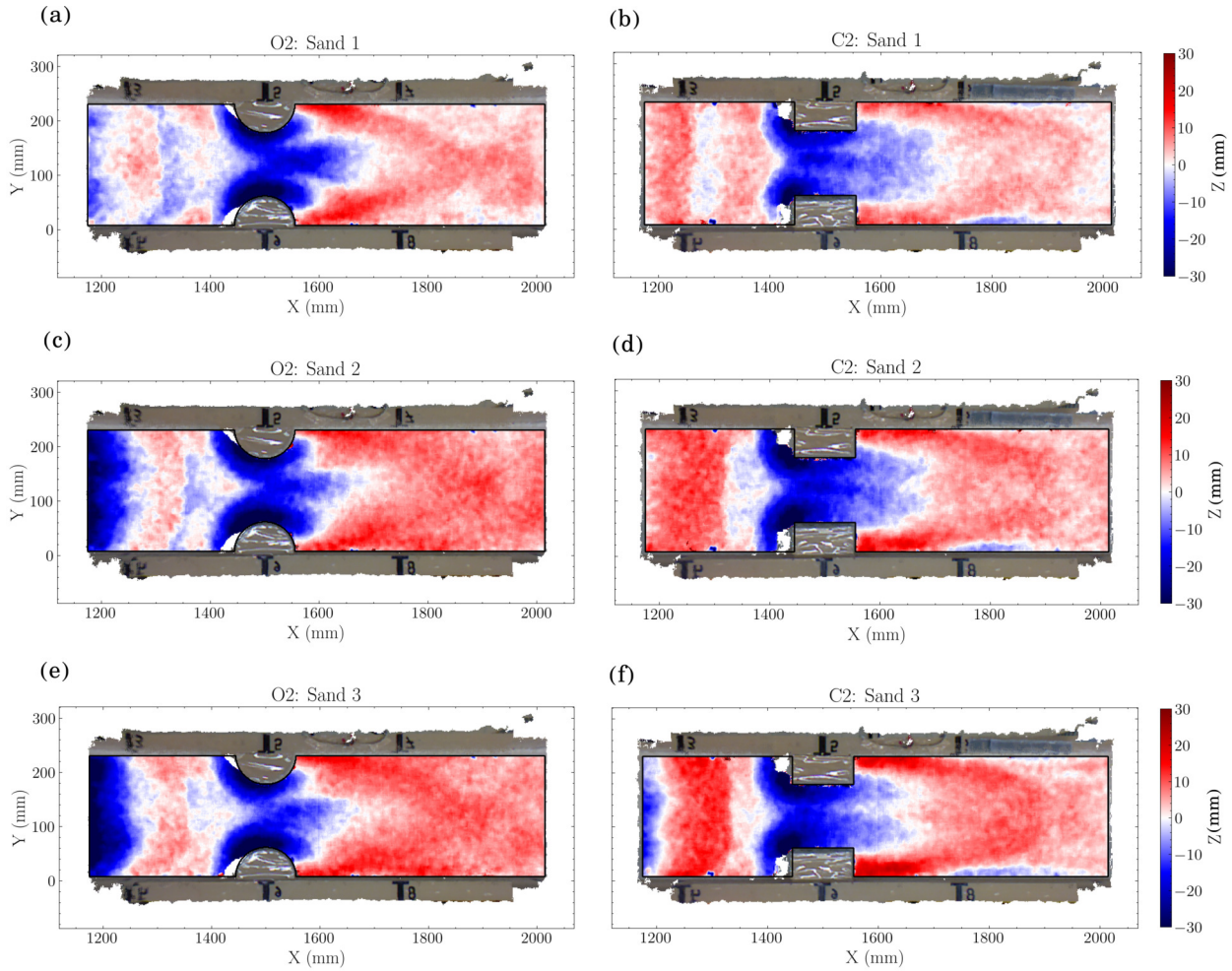

Figure 13 Dataset 2D maps: Evolution of scour and deposition for configurations O2 (left) and C2 (right). The rows, from top to bottom, show the final bedform after the first (a)-(b), second (c)-(d), and third (e)-(f) consecutive dam breaks, respectively. Flow is from left to right.

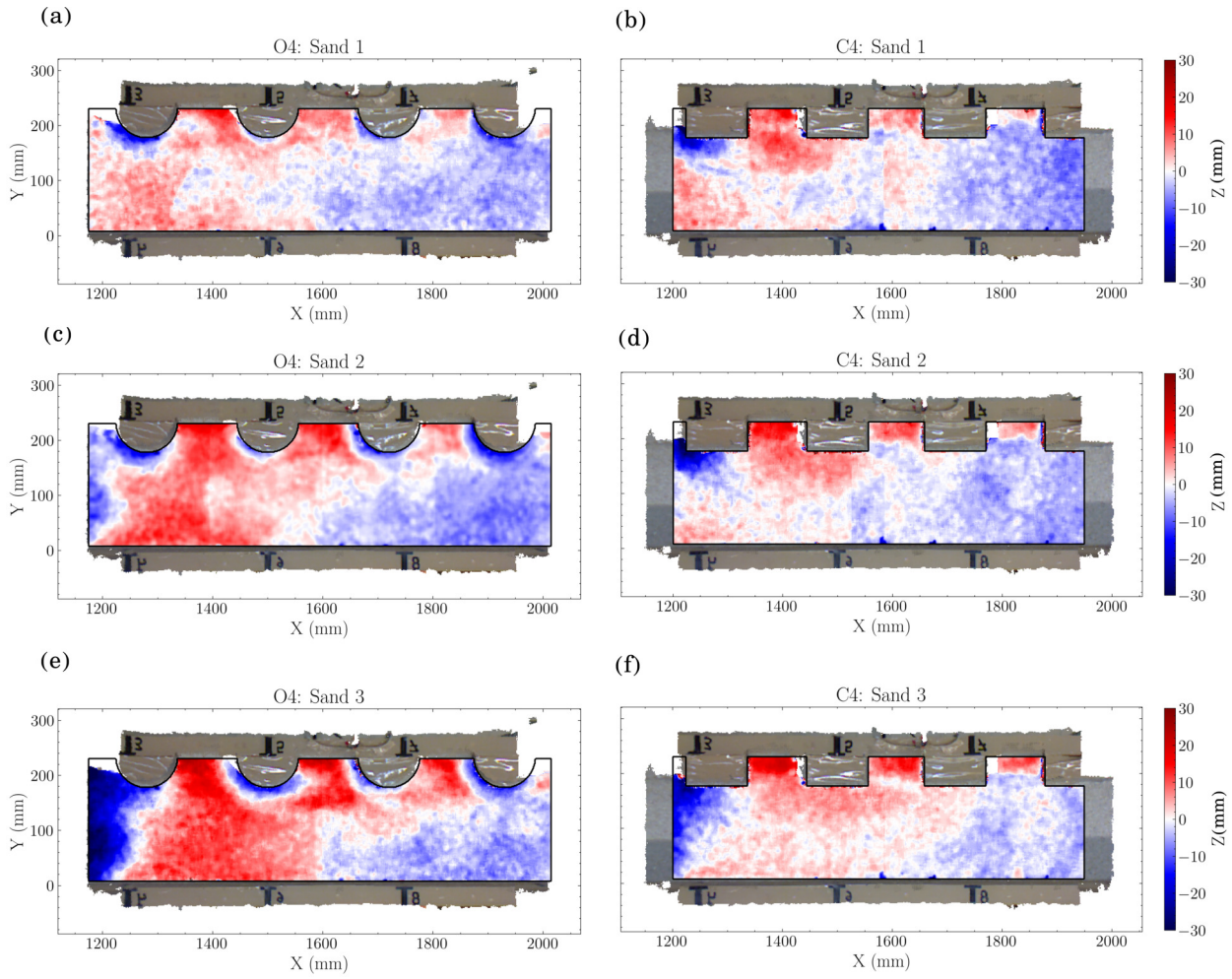

Figure 14 Dataset 2D maps: Evolution of scour and deposition for configurations O4 (left) and C4 (right). The rows, from top to bottom, show the final bedform after the first (a)-(b), second (c)-(d), and third (e)-(f) consecutive dam breaks, respectively. Flow is from left to right.

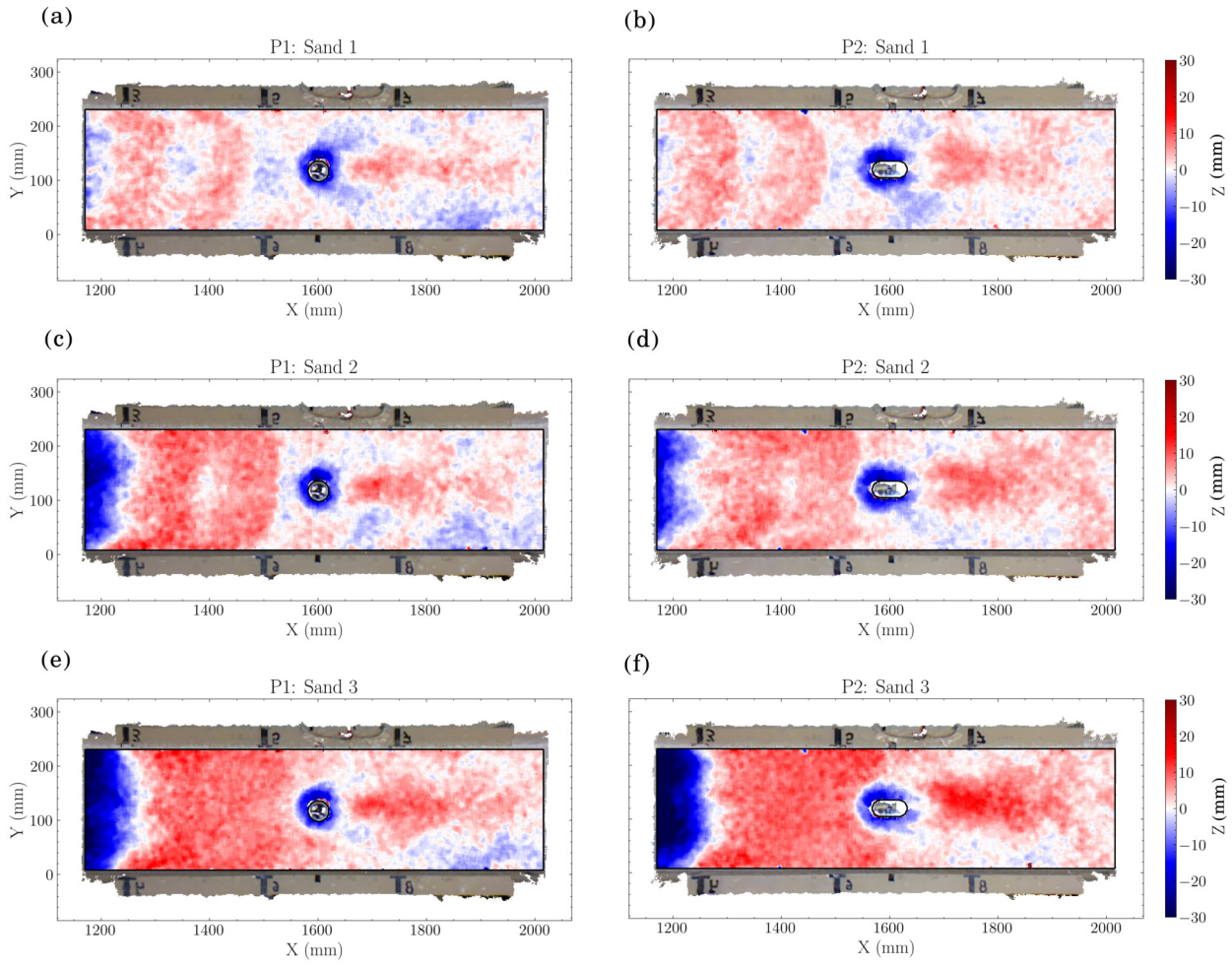

Figure 15 Dataset 2D maps: Evolution of scour and deposition for configurations P1 (left) and P2 (right). The rows, from top to bottom, show the final bedform after the first (a)-(b), second (c)-(d), and third (e)-(f) consecutive dam breaks, respectively. Flow is from left to right.

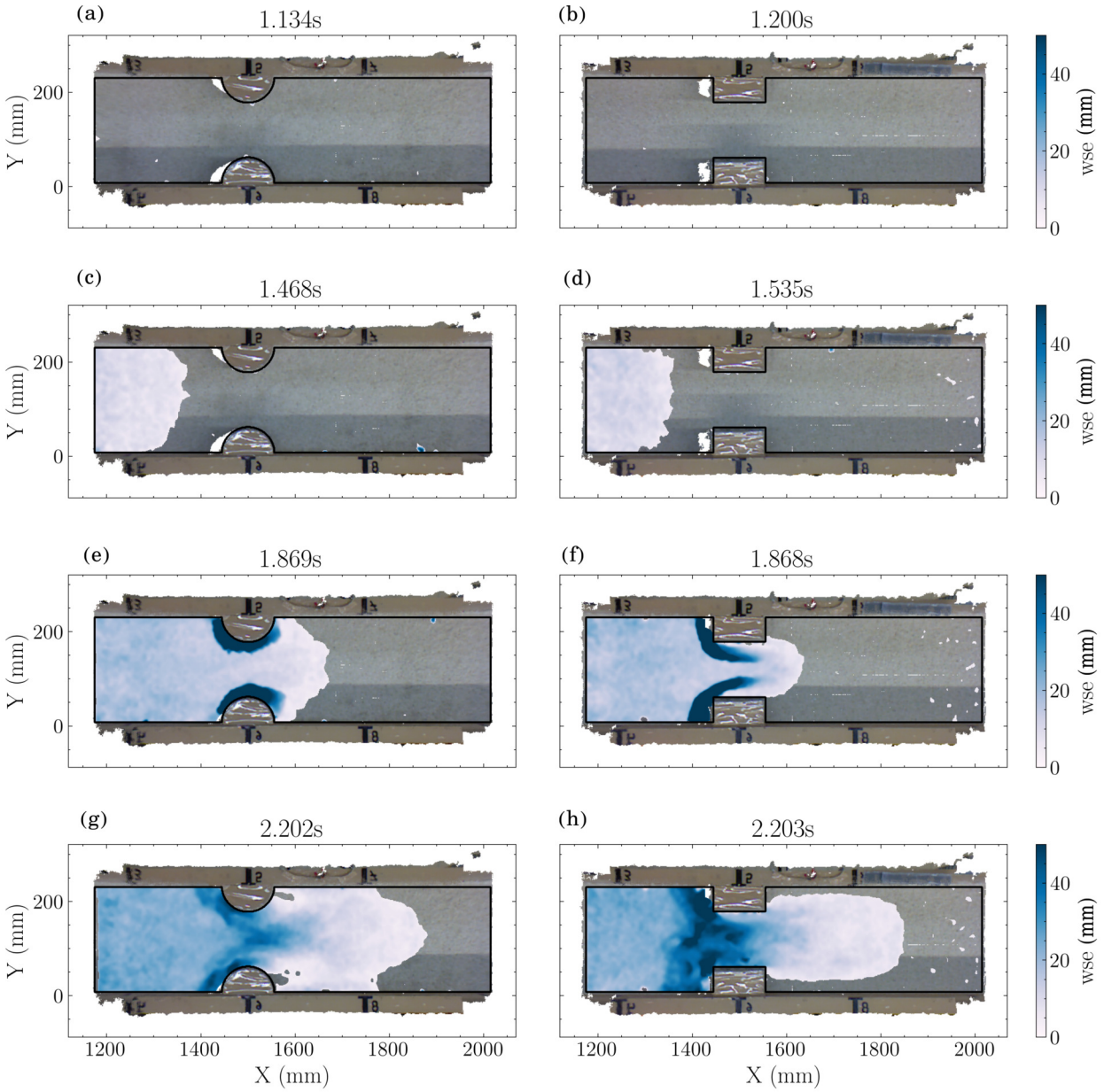

Figure 16 Water Surface Elevation (WSE) evolution for the O2 (left) and C2 (right) narrowing configurations for the first dambreak. For each configuration, four snapshots show the WSE at consecutive moments in time, arranged from top to bottom. Flow is from left to right.

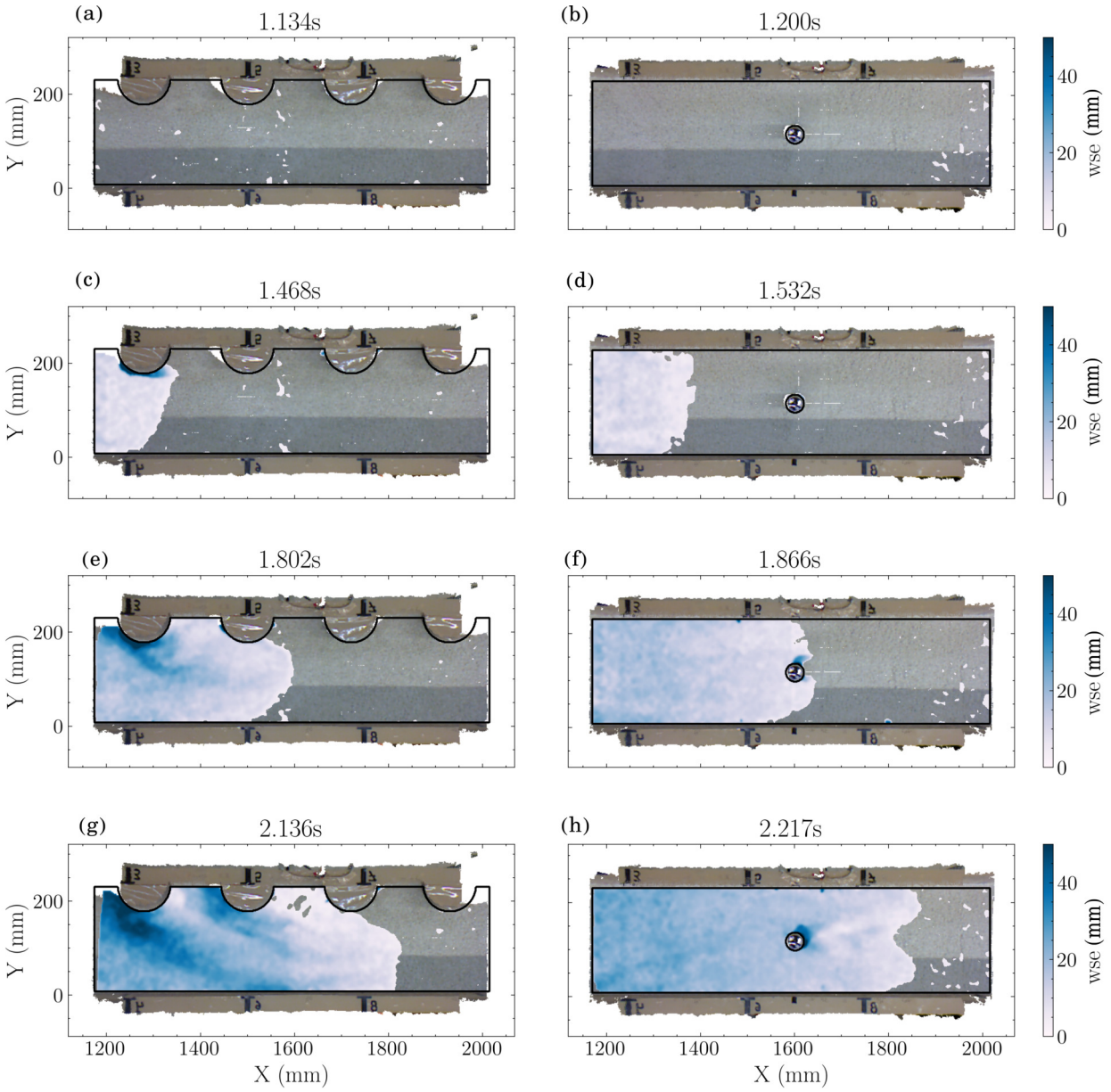

Figure 17 Comparison of Water Surface Elevation (WSE) during the first dam-break wave for the O4 and P1 obstacle configurations. Flow is from left to right in all panels. WSE snapshots for the O4 (a), (c), (e), (g) configuration, shown at $t = 1.134$, 1.468, 1.802, and 2.136 s. WSE snapshots for the P1 configuration, shown at $t = 1.200$ (b), 1.532 (d), 1.866 (f), and 2.217 s (h). The snapshots in each panel are arranged chronologically from top to bottom.

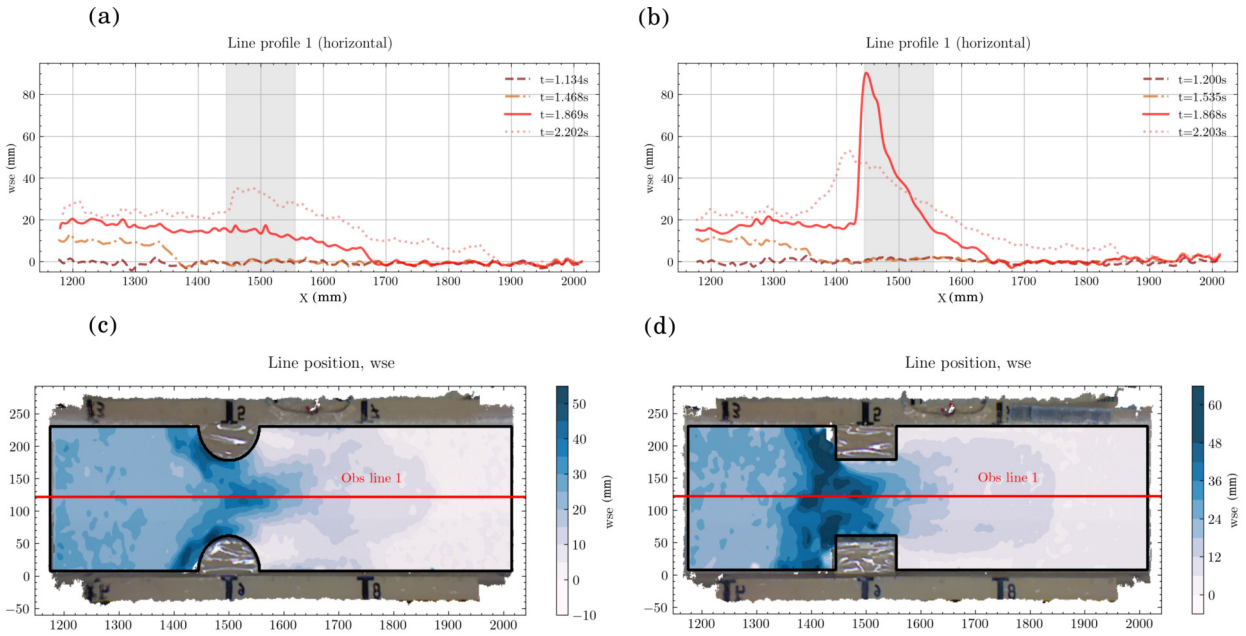

Figure 18 Comparison of Water Surface Elevation (WSE) profiles. The top panels show the longitudinal WSE profiles for the O2 case (a) and the C2 case (b). The bottom panels show the location of the measurement transects for O2 (c) and C2 (d).

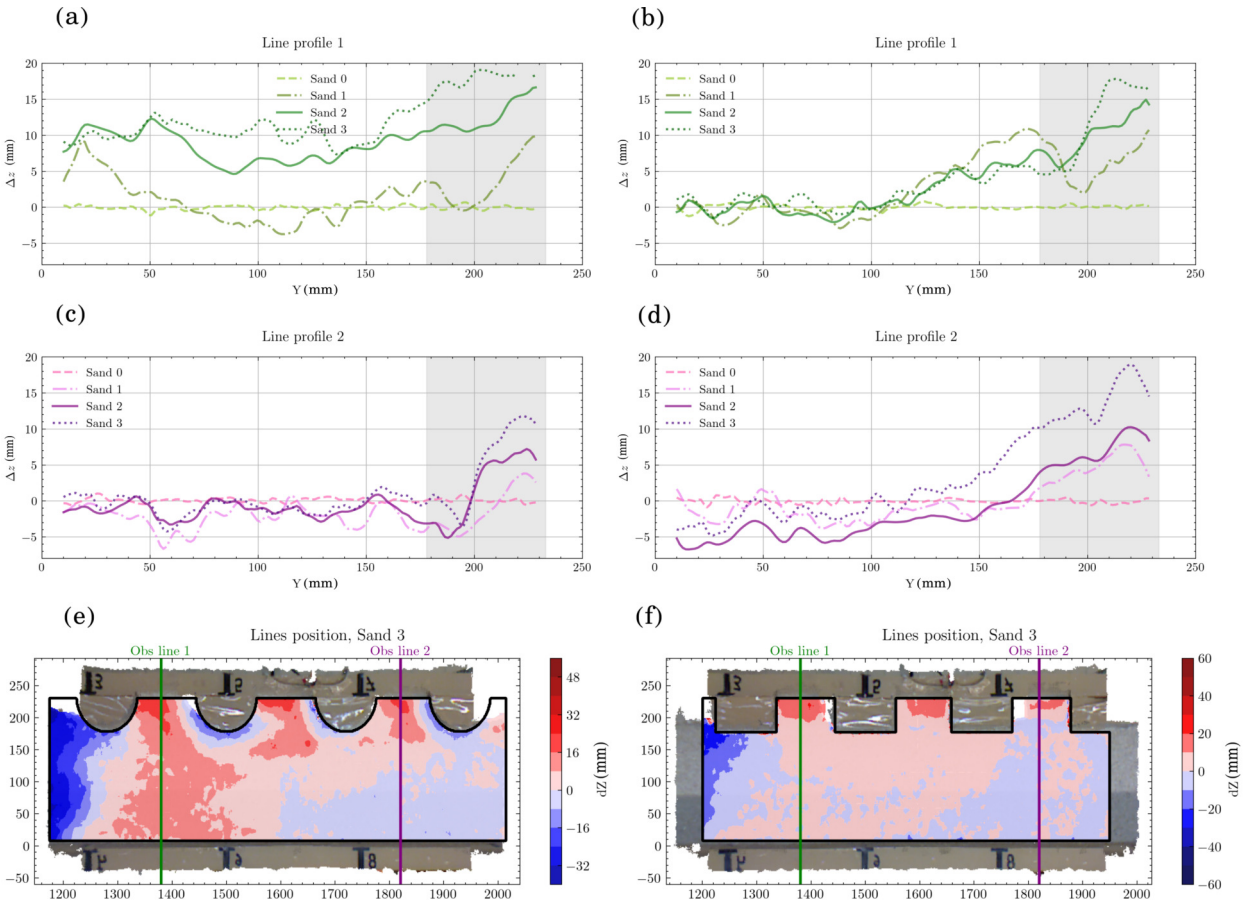

Figure 19 Comparison of final bed morphology for experimental cases O4 (left column) and C4 (right column). Panels (a) and (b) show the bed profile along Line 1. Panels (c) and (d) show the bed profile along Line 2. The locations of the measurement lines are shown in panels (e) and (f).

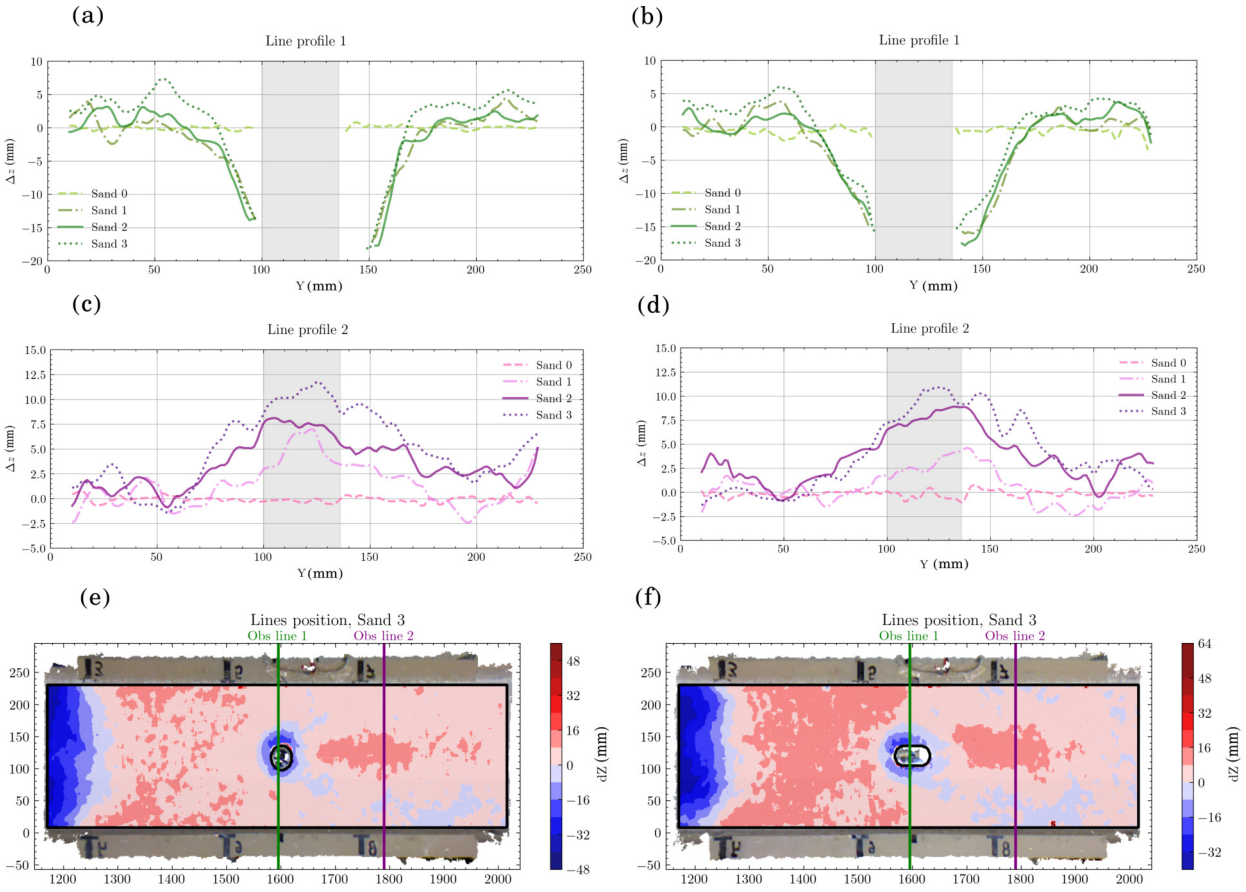

Figure 20 Comparison of final bed morphology for experimental cases P1 (left column) and P2 (right column). Panels (a) and (b) show the bed profile along Line 1. Panels (c) and (d) show the bed profile along Line 2. The locations of the measurement lines are shown in panels (e) and (f).

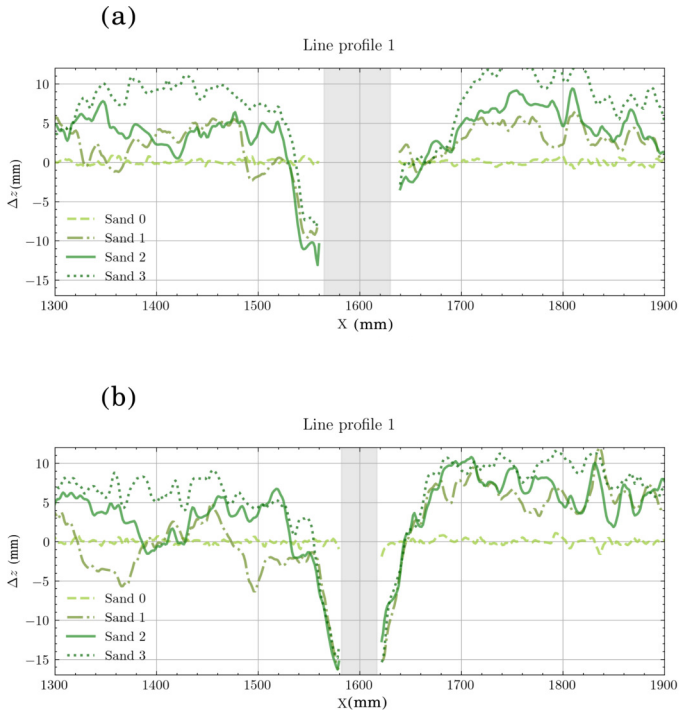

Figure 21 Evolution of longitudinal scour profiles along the flume centerline for the P1 (a) and P2 (b) configurations. In each plot, different line styles represent the bed profile after each of the three consecutive dam breaks. The gray shaded area indicates the position of the obstacle.

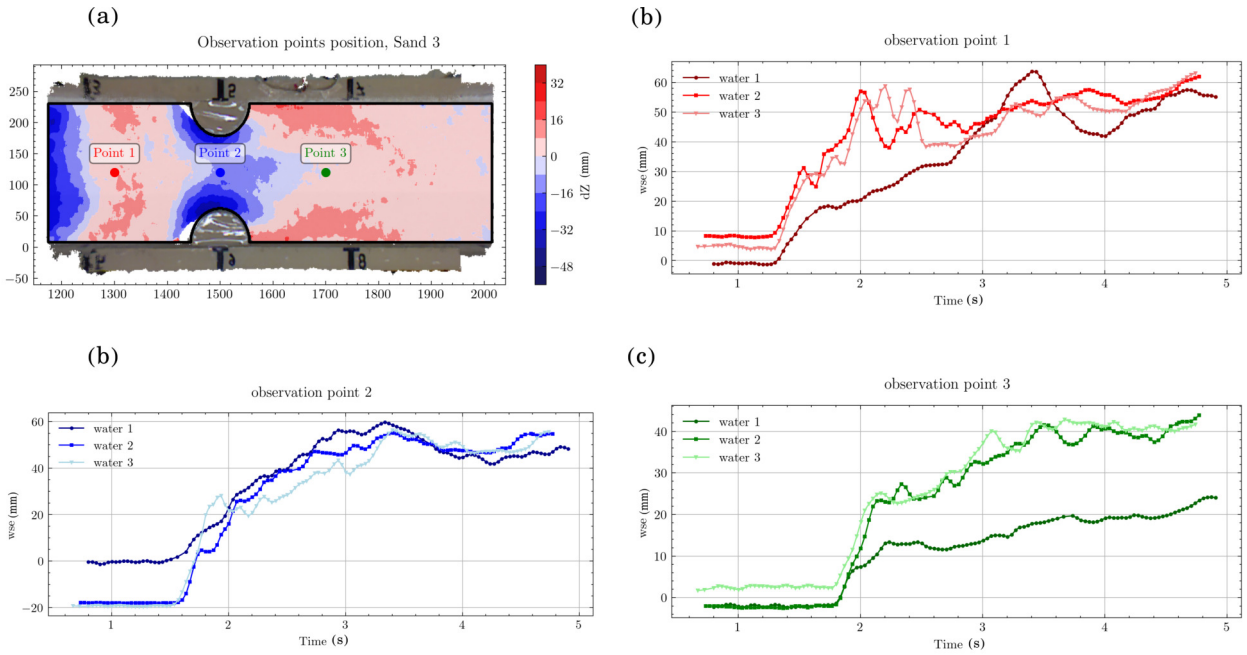

Figure 22 Time evolution probe analysis in the O2 case. Transient Water Surface Elevation is shown at point 1 (b, red), point 2 (c, blue), and point 3 (d, green). In each subplot, the different lines correspond to each of the three consecutive dambreaks.

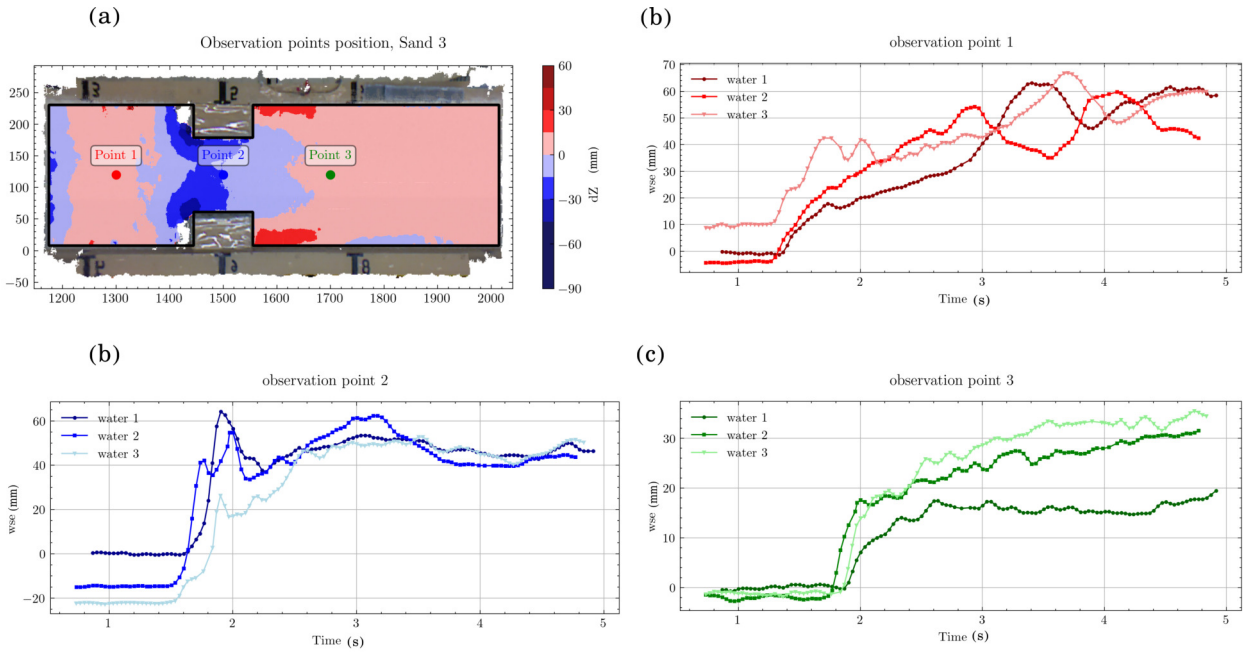

Figure 23 Time evolution probe analysis in the C2 case. Transient Water Surface Elevation is shown at point 1 (b, red), point 2 (c, blue), and point 3 (d, green). In each subplot, the different lines correspond to each of the three consecutive dambreaks.

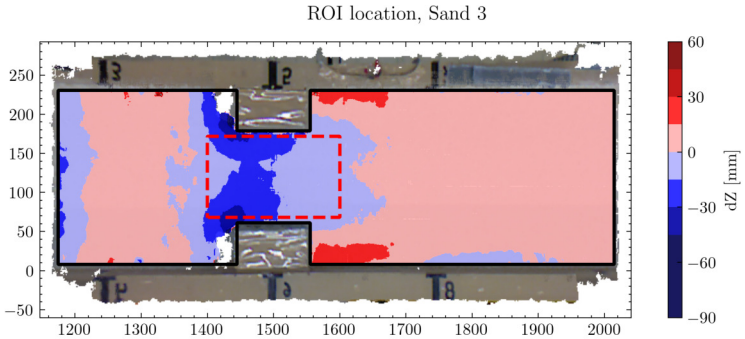

Figure 24 Location of the Region of Interest (ROI), indicated by the red dashed line. The background shows the final bed state of the C2 experiment (run `sand3`) for visual reference.